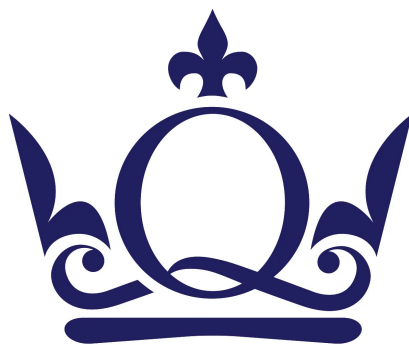


# Short-Range Electrostatics in Molecular Systems:

A Computational and Analytic Approach

By Yonis Hassan



Queen Mary University of London  
Department of Physics and Astronomy

# Contents

<b>1</b>	<b>Introduction</b>	<b>7</b>
1.1	The Ubiquity of Electrostatic Interactions . . . . .	7
1.2	Types of Electrostatic Interactions . . . . .	7
1.2.1	The Breakdown of Classical Models . . . . .	7
1.3	Bridging Classical and Quantum Electrostatics . . . . .	8
1.3.1	The Quantum Advantage . . . . .	8
1.3.2	Research Rationale . . . . .	9
1.4	Key Questions . . . . .	9
1.5	Background Information . . . . .	9
1.6	Types of Electrostatic Interactions . . . . .	9
1.6.1	Ion-Ion Interactions . . . . .	9
1.6.2	Ion-Dipole Interactions . . . . .	10
1.6.3	Dipole-Dipole Interactions . . . . .	10
1.6.4	Point Dipole-Point Dipole Interactions . . . . .	10
1.6.5	Higher-Order Multipoles . . . . .	12
1.6.6	Classical Models . . . . .	13
1.6.7	Quantum Mechanical Methods . . . . .	13
1.6.8	Charge Penetration . . . . .	13
1.6.9	Bridging Classical and Quantum . . . . .	13
1.6.10	Applications . . . . .	14
<b>2</b>	<b>Literature Review</b>	<b>15</b>
2.1	Introduction . . . . .	15
2.2	Existing Charge-Penetration Corrections . . . . .	15
2.2.1	Empirical Damping in Multipole Force Fields . . . . .	15
2.2.2	Density-Based & Gaussian Multipole Models . . . . .	15
2.2.3	QM/MM Screening & Partitioning . . . . .	16
2.2.4	Implicit-Solvent & Continuum Corrections . . . . .	16
2.3	Conclusion . . . . .	17
<b>3</b>	<b>Computational Methods</b>	<b>19</b>
3.1	Molecular System Setup . . . . .	19
3.2	How did we define the ion-dipole system? . . . . .	21
3.3	How did we define the physical dipole-dipole system? . . . . .	22
3.4	How did we define the point-dipole system? . . . . .	23

3.5	Quantum Interaction Energy Calculation (SAPT0)	24
3.5.1	Justification of SAPT <sub>0</sub> Over Higher-Order Methods	24
3.5.2	Classical Coulombic Interaction Energy	24
3.5.3	Electrostatic Penetration Energy	25
3.5.4	Visualisation	25
<b>4</b>	<b>Results</b>	<b>27</b>
4.1	Physical Dipole-Dipole Interactions	27
4.2	Orientation 1: Parallel ( $\theta = 0^\circ$ )	27
4.2.1	Orientation 2: Antiparallel ( $\theta = 180^\circ$ )	28
4.3	Ion-Dipole Interactions	31
4.4	Orientation 1: Parallel ( $\theta = 0^\circ$ , H closer to H <sup>-</sup> )	32
4.4.1	Classical Results	32
4.4.2	SAPT0 Results	33
4.5	Orientation 2: Anti-Parallel $\theta = 180^\circ$ (F closer to H <sup>-</sup> )	33
4.5.1	Classical Results	33
4.5.2	SAPT0 Results	33
4.6	Orientation 3: Perpendicular $\theta = 90^\circ$	33
4.6.1	Classical Results	33
4.6.2	SAPT0 Results	34
4.7	Point Dipole-Dipole Interactions	34
4.7.1	Orientation 1: Parallel ( $\theta = 0^\circ$ )	35
4.7.2	Orientation 2: Antiparallel( $\theta = 180^\circ$ )	35
4.7.3	Orientation 3: Perpendicular( $\theta = 90^\circ$ )	35
4.8	Charge penetration	36
4.8.1	Ion-Dipole Penetration	36
4.8.2	Physical Dipole Penetration	37
4.8.3	Point-Dipole Penetration	37
<b>5</b>	<b>Discussion</b>	<b>40</b>
5.1	Mechanisms Behind Breakdown	40
5.2	Distance Thresholds	41
5.2.1	Orientation Sensitivity	42
5.3	Insights from Exponential Decay	42
5.4	Analysis of SAPT0 Electrostatic Decomposition	43
5.4.1	Connection to Orbital Tails	43
5.4.2	Origins of Orientation-Dependent Penetration	44
5.5	Implications for Force-Field Design	44
5.5.1	Need for Overlap-Dependent Damping	45
5.5.2	Polarisable vs. Fixed-Charge Models	45
5.6	Biological Significance	46
5.6.1	Protein Folding	46
5.7	Limitations & Future Work	46
5.7.1	Modeling Extensions	46
5.7.2	Implications of Quantum-Induced Bonding	47

<b>6</b>	<b>Conclusion</b>	<b>48</b>
6.1	Did We Achieve Our Original Goal? . . . . .	48
6.2	Key Findings . . . . .	48
6.3	Methodological Considerations . . . . .	48
6.4	Novel Insights . . . . .	49
6.5	Future Directions . . . . .	49
6.6	Concluding Remarks . . . . .	49
<b>A</b>	<b>Mathematical Foundations of Electrostatic Models</b>	<b>50</b>
A.1	Taylor Expansion in Electrostatics . . . . .	50
A.2	Classical Derivations and Angular Dependence . . . . .	50
A.3	Structure of SAPT Calculations . . . . .	51
B.4	Numerical Considerations . . . . .	51
A.4	From the Schrödinger Equation to SAPT . . . . .	51
A.4.1	The Time-Independent Schrödinger Equation . . . . .	51
A.4.2	Perturbation Theory as an Approximation . . . . .	52
<b>B</b>	<b>Comprehensive Derivation of Ion-Dipole Interactions</b>	<b>53</b>
B.0.1	Foundational Electrostatics . . . . .	53
B.0.2	Dipole Moment Definition (Eq. 4.1) . . . . .	53
B.0.3	Dipole Self-Energy (Eq. 4.2) . . . . .	53
B.0.4	Exact Ion-Dipole Interaction (Eq. 4.3) . . . . .	54
B.0.5	Taylor Expansion Details . . . . .	54
B.0.6	Point Dipole Approximation (Eq. 4.5) . . . . .	54
B.0.7	Numerical Example . . . . .	55
B.0.8	Quantum Mechanical Connection . . . . .	55
B.0.9	Torque Derivation . . . . .	55
<b>C</b>	<b>Multipole Interactions Classical and Quantum comparisons</b>	<b>56</b>
C.1	Extended Derivation of Ion-Dipole Interactions . . . . .	56
C.1.1	Multipole Expansion (Beyond Dipole Approximation) . . . . .	56
C.1.2	Finite-Size Corrections . . . . .	56
C.1.3	Dielectric Continuum Theory . . . . .	56
C.1.4	Quantum Mechanical Perturbation Theory . . . . .	57
C.1.5	Molecular Dynamics Verification . . . . .	57
C.1.6	Angle-Dependent Force Derivation . . . . .	57
C.1.7	Relativistic Corrections (for completeness) . . . . .	57
C.1.8	Comparison to van der Waals Interaction . . . . .	57
C.1.9	Experimental Validation . . . . .	58

# List of Figures

1.1	Schematic of the four IQF electrostatic contributions: three penetration terms (dark blue) and the intra-basin interaction (dark green), highlighting the distinction between the zeroth-order pairwise term $E_{\text{ele}}^{0,AB}$ and the penetration components. Adapted from Jiménez-Grávalos and Suárez [6]. . . . .	8
1.2	Dipole-dipole interaction showing finite-size effects (solid) vs. point dipole approximation (dashed). Adapted from [4, Fig. 4.3]. . . . .	11
2.1	Electrostatic interaction energy versus closest-atom separation for water–water (top row), benzene–benzene $\pi$ – $\pi$ (middle row), and benzene–benzene T-shaped (bottom row) dimers. SAPT <sub>0</sub> results are shown in blue, uncorrected multipoles in green, and multipoles with valence- $\alpha$ charge-penetration correction in red. The vertical dashed line indicates the equilibrium separation for each complex [14]. . . . .	16
2.2	Charge–dipole interaction energy in vacuum between a unit charge $e$ and a 1 D dipole at orientations $\theta = 0^\circ, 90^\circ, 180^\circ$ . Solid lines show exact results for finite dipoles ( $\ell = 0.02$ nm and 0.10 nm); dashed lines are the point-dipole limit ( $\ell = 0$ ). Note that at $r \approx 0.3$ –0.4 nm the interaction magnitude greatly exceeds $kT$ at 300 K, [4] . . . . .	18
3.1	Different orientations of hydrogen fluoride dipoles interacting. Used as a visual aid during my research. . . . .	20
3.2	Comparison of classical and quantum electrostatic interaction energies. . . . .	26
4.1	Parallel dipole–dipole interaction energies . . . . .	28
4.2	Electrostatic interaction energy $w(r)$ between two HF dipoles in the antiparallel configuration ( $\theta = 180^\circ$ ), plotted as a function of centre-to-centre separation $r$ . The dashed blue curve shows the classical point-dipole prediction, and the solid red curve shows the SAPT <sub>0</sub> reference energy. . . . .	29
4.3	Electrostatic interaction energy $W(r)$ versus HF–HF separation $r$ for the perpendicular dipole–dipole alignment ( $\theta = 90^\circ, \phi = 0^\circ$ ). Dashed blue line indicates the classical prediction (near zero), and the solid red line shows SAPT <sub>0</sub> reference calculations. . . . .	30
4.4	Electrostatic interaction energy $W(r)$ for the opposite perpendicular dipole–dipole alignment ( $\theta = 90^\circ, \phi = 180^\circ$ ). Dashed blue line indicates the classical prediction (near zero), and the solid red line shows the SAPT <sub>0</sub> reference calculation. . . . .	31

4.5	Electrostatic interaction energy $W(r)$ for the HF-H <sup>-</sup> ion-dipole system plotted as a function of intermolecular separation $r$ . The dashed blue line represents the classical idealized point-dipole model, the solid green line corresponds to the classical physical-dipole model (discrete charges separated by a finite bond length), and the solid black line provides the SAPT0 quantum reference calculation. . . . .	32
4.6	Electrostatic interaction energy versus separation distance for two dipoles in the perpendicular ( $\theta = 90^\circ$ ) alignment, comparing the classical point-dipole prediction (dashed line) with SAPT0 quantum calculations (solid line). . . . .	34
4.7	Semi-log plot of the absolute penetration energy $ \Delta E_{\text{pen}}(r)  =  E_{\text{SAPT0}}(r) - E_{\text{classical}}(r) $ as a function of HF-H <sup>-</sup> separation $r$ in the collinear orientation ( $\theta = 0^\circ$ ). The linear fit on this plot indicates an exponential decay of the penetration correction with distance. . . . .	36
4.8	Semi-log plot of the absolute penetration energy $ \Delta E_{\text{pen}}(r)  =  E_{\text{SAPT0}}(r) - E_{\text{Coulomb}}(r) $ as a function of dipole-dipole separation $r$ in the parallel alignment ( $\theta = 0^\circ$ ). The straight-line behaviour on this scale indicates an approximately exponential decay of the penetration correction. . . . .	37
4.9	Log plot of penetration energy in the perpendicular orientation. . . . .	38

# Abstract

This dissertation compares quantum mechanical calculations directly with classical electrostatic models to assess their accuracy. Although classical point-charge approximations agree well with quantum methods at larger separations, they are unable to capture short-range interactions ( $<0.5$  nm), even though electrostatic forces dominate molecular behaviour. We create useful corrections to classical force fields in order to close this gap. Using symmetry-adapted perturbation theory (SAPT0), quantum interaction energies were calculated, and Coulomb's law was used to calculate their classical counterparts from point-charge distributions. Key short-range interactions are consistently understated by classical models, according to our analysis, which shows systematic, orientation-dependent discrepancies. We suggest a corrective framework based on physics that greatly enhances agreement with quantum benchmarks. This work improves the accuracy of molecular simulations while preserving computational efficiency by tackling these basic constraints. The ensuing enhancements can be applied to materials science and bio-molecular modelling.

# Chapter 1

## Introduction

### 1.1 The Ubiquity of Electrostatic Interactions

From the high melting points of ionic crystals to biomolecular recognition, electrostatic forces control events across large scales. They dictate ion solvation, stabilise protein structures, and drive DNA base pairing—highlighting their central role in chemistry, biology, and materials science [3]. These interactions arise from Coulomb’s law:

$$F = k_e \frac{q_1 q_2}{r^2}, \quad (1.1)$$

still, even neutral molecules show significant polarisation effects caused by partial charges. ( $\delta^+$ ,  $\delta^-$ ) or permanent dipoles ( $\mu = q\ell$ ), enabling forces like hydrogen bonding.

### 1.2 Types of Electrostatic Interactions

This study examines three fundamental electrostatic interactions using quantum-mechanical computations and energy decomposition analyses. First, we consider *point-dipole–point-dipole* interactions, which probe atomic-scale charge asymmetries via the atomic dipoles

$$m_{A,x}, m_{A,y}$$

derived from the Cartesian second moments of the monomer electron density. Second, we investigate *permanent dipole–dipole* interactions, characterized by their angular orientation dependence and a canonical  $r^{-3}$  distance scaling. Specific geometries (parallel, antiparallel, perpendicular) are benchmarked against SAPT reference values. Finally, we analyse *ion–dipole* interactions, whose  $r^{-2}$  scaling yields the strongest electrostatic attraction at moderate distances, a key factor in polar solvation phenomena. Throughout, we employ *ab initio* electronic-structure calculations and symmetry-adapted perturbation theory to quantify relative interaction strengths, orientation sensitivities, and distance-dependent behaviour.

#### 1.2.1 The Breakdown of Classical Models

Although classical point-charge approximations perform well at long distances, they depart from quantum reality at sub-van der Waals distances. This discrepancy arises from charge penetration



electron cloud overlap that reduces repulsion—which classical multipole expansions fail to capture without empirical damping functions, this is illustrated in 1.1.

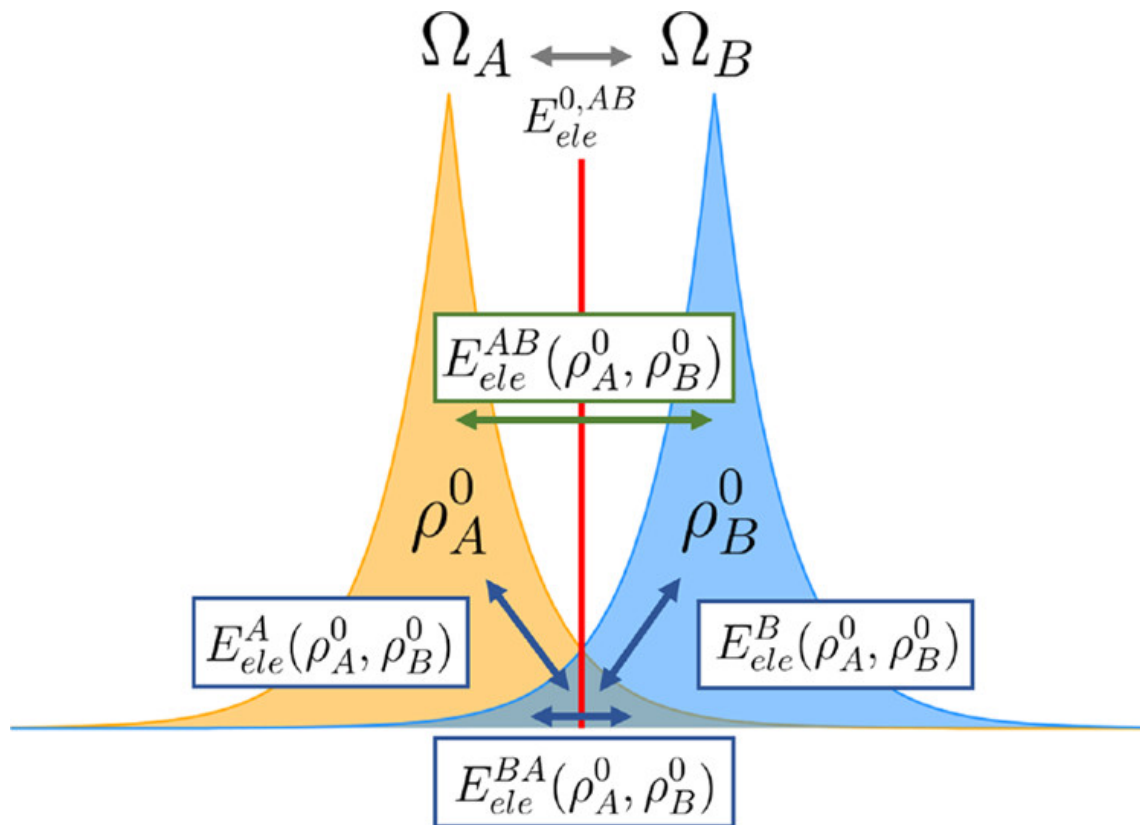


Figure 1.1: Schematic of the four IQF electrostatic contributions: three penetration terms (dark blue) and the intra-basin interaction (dark green), highlighting the distinction between the zeroth-order pairwise term  $E_{ele}^{0,AB}$  and the penetration components. Adapted from Jiménez-Grávalos and Suárez [6].

## 1.3 Bridging Classical and Quantum Electrostatics

### 1.3.1 The Quantum Advantage

Quantum methods like Symmetry-Adapted Perturbation Theory (SAPT) naturally incorporate charge penetration. Using Hartree-Fock densities, the lowest-order variant SAPT0 separates interaction energies into physically interpretable components—electrostatics, exchange-repulsion, induction, dispersion. Unlike classical models, it considers electron cloud overlap without ad hoc adjustments. It also has the benefit of being the computationally cheapest variant of SAPT making it very practical.

### 1.3.2 Research Rationale

This work addresses the gap between classical efficiency and quantum accuracy by:

- Measuring classical-quantum differences over intermolecular distances
- Creating SAPT0-informed adjustments for classical force fields
- Validating against high-level benchmarks for non-covalent complexes

## 1.4 Key Questions

- In what ways do classical point-charge models differ from SAPT0 electrostatic energies?
- At what limits do charge penetration effects start to have any significance?
- What analytic corrections can bridge this gap while preserving computational practicality?

Reconciling these methods will help to improve the accuracy of molecular simulations in drug design, materials science, and more.

## 1.5 Background Information

In this section we will give some background information on the topic in order to understand the study in depth. In case you weren't aware electrostatic interactions are forces between charged entities. In molecular systems, these arise from Coulomb's law (1.1), a more detailed version of coulombs law can be seen in the appendix, (B.1).

## 1.6 Types of Electrostatic Interactions

The multipole order of the interacting species permits one to methodically categorise electrostatic interactions. The basic kinds and their typical distance dependencies are covered in this part.

### 1.6.1 Ion-Ion Interactions

The simplest case involves two point charges  $q_1$  and  $q_2$ :

$$U_{\text{ion-ion}} = \frac{q_1 q_2}{4\pi\epsilon_0\epsilon r}, \quad (1.2)$$

where  $\epsilon$  is the medium's dielectric constant. This Coulombic interaction decays as  $1/r$  and is isotropic. There are times in this study where the constant  $4\pi\epsilon_0\epsilon r$  is omitted and this is due to us using atomic units (A.U) or hartrees (H) as our units of energy. At times it isn't stated explicitly but rather implied.

### 1.6.2 Ion-Dipole Interactions

For a point charge  $Q$  interacting with a dipole  $\mu$  at angle  $\theta$ .

The exact energy expression: [4]

$$w(r) = -\frac{Qq}{4\pi\epsilon_0\epsilon} \left( \frac{1}{AB} - \frac{1}{AC} \right), \quad (1.3)$$

where  $AB = r - \frac{1}{2}\ell \cos \theta$  and  $AC = r + \frac{1}{2}\ell \cos \theta$ . In the point dipole limit ( $r \gg \ell$ ):

$$w(r, \theta) = -\frac{Q\mu \cos \theta}{4\pi\epsilon_0\epsilon r^2} = -\mu E(r) \cos \theta, \quad (1.4)$$

where  $E(r) = Q/(4\pi\epsilon_0\epsilon r^2)$ . Key features:

- $1/r^2$  distance dependence (stronger than dipole-dipole)
- Orientation-dependent ( $\cos \theta$  term)
- Dominates in ionic solvation (e.g.,  $\text{Na}^+ - \text{H}_2\text{O}$ )

### 1.6.3 Dipole-Dipole Interactions

The interaction between two dipoles  $\mu_1$  and  $\mu_2$  depends on their relative orientations ( $\theta_1, \theta_2, \phi$ ):

$$U = -\frac{\mu_1\mu_2}{4\pi\epsilon_0\epsilon r^3} [2 \cos \theta_1 \cos \theta_2 - \sin \theta_1 \sin \theta_2 \cos \phi]. \quad (1.5)$$

Special cases from [4, Ch. 4]:

- *In-line alignment*:  $U = -2\mu_1\mu_2/(4\pi\epsilon_0\epsilon r^3)$
- *Parallel alignment*:  $U = -\mu_1\mu_2/(4\pi\epsilon_0\epsilon r^3)$

**Thermal Averaging** In fluids, rotational averaging yields the Keesom interaction:

$$\langle U(r) \rangle = -\frac{\mu_1^2 \mu_2^2}{3(4\pi\epsilon_0\epsilon)^2 k_B T r^6}. \quad (1.6)$$

### 1.6.4 Point Dipole-Point Dipole Interactions

In the theoretical treatment of molecular interactions, point dipoles serve as a fundamental model for understanding electrostatic effects. When two atoms or molecules are represented as point dipoles with moments  $\mu_1$  and  $\mu_2$ , their interaction energy depends on both separation distance  $r$  and relative orientation.

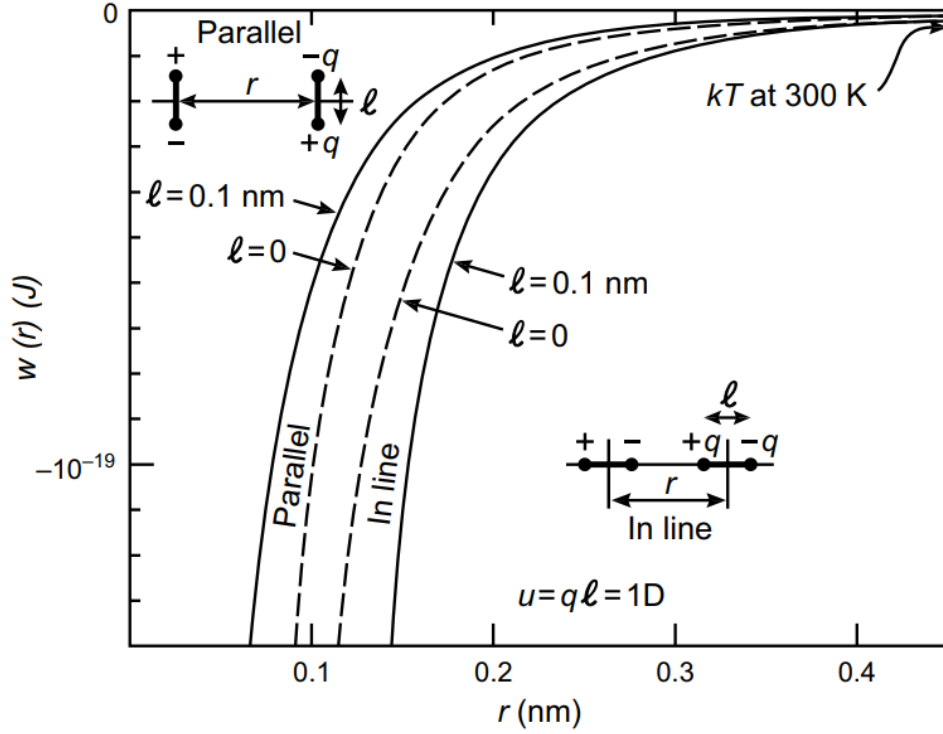


Figure 1.2: Dipole-dipole interaction showing finite-size effects (solid) vs. point dipole approximation (dashed). Adapted from [4, Fig. 4.3].

### Definition of Atomic Point Dipoles

For planar molecules (lying in the  $xy$ -plane), the in-plane components of the atomic point dipole on atom  $A$  can be uniquely determined from the molecular second moments [2]:

$$m_{A,x} = 2 \frac{\partial M_{xz}}{\partial Z_A}; \quad m_{A,y} = 2 \frac{\partial M_{yz}}{\partial Z_A} \quad (1.7)$$

where:

- $M_{\alpha z}$  are elements of the molecular second moment tensor (e.g.,  $M_{xz} = \int \rho(r) xz d^3r$ )
- $Z_A$  is the out-of-plane ( $z$ ) coordinate of atom  $A$
- The factor of 2 arises from molecular-to-atomic decomposition [2]

By symmetry, the out-of-plane component vanishes:  $m_{A,z} = 0$ .

## Interaction Energy

The interaction energy between two point dipoles follows the general form [4]:

$$w(r, \theta) = -\frac{\mu_1 \mu_2}{4\pi\epsilon_0 \epsilon r^3} (2 \cos \theta_1 \cos \theta_2 - \sin \theta_1 \sin \theta_2 \cos \phi) \quad (1.8)$$

where  $\theta_1$  and  $\theta_2$  are the angles each dipole makes with the intermolecular axis, and  $\phi$  is their dihedral angle, similar to the physical dipole. In the special case where one dipole is a point charge  $Q$  and the other a point dipole  $\mu$ , the interaction reduces to [4]:

$$w(r, \theta) = -\frac{Q\mu \cos \theta}{4\pi\epsilon_0 \epsilon r^2} = -\mu \cdot E(r) \quad (1.9)$$

where  $E(r) = Q/(4\pi\epsilon_0 \epsilon r^2)$  is the electric field of the point charge.

## Physical Interpretation and Validation

The atomic point dipoles defined via Eq. (1) exactly reproduce:

- The molecule’s overall dipole and quadrupole moments
- The far-field electrostatic potential
- The correct long-range atom-atom electrostatic force constants [2]

These dipoles show up naturally in the asymptotic shape of intermolecular force constants:

$$H_{AB} \approx -\frac{6}{R^4} (q_A m_B - q_B m_A) + \dots \quad (1.10)$$

providing a rigorous test of their physical validity [2]. The use of out-of-plane derivatives ensures these are true static multipoles, uncontaminated by intramolecular charge flux effects [2].

### 1.6.5 Higher-Order Multipoles

For completeness, the general multipole expansion of the electrostatic potential:

$$\Phi(\mathbf{r}) = \frac{1}{4\pi\epsilon_0} \left[ \frac{Q}{r} + \frac{\mathbf{p} \cdot \hat{\mathbf{r}}}{r^2} + \frac{1}{2r^3} \sum_{i,j} Q_{ij} \hat{r}_i \hat{r}_j + \dots \right], \quad (1.11)$$

where  $Q$  is the monopole (charge),  $\mathbf{p}$  the dipole moment, and  $Q_{ij}$  the quadrupole tensor. Higher-order terms scale as  $1/r^{n+1}$  for the  $2^n$ -pole.

**Limitations** In this work we restrict our treatment to fixed point-charge and point-dipole models without delving into higher-order multipole moments or the effects of rotational (Keesom) averaging in solution. Instead, we focus exclusively on SAPT<sub>0</sub> calculations of static dimer geometries, acknowledging that SAPT<sub>0</sub> does not include explicit penetration-corrected multipoles, higher-order induction/dispersion couplings, or thermal averaging of orientations. This choice reflects a balance between accuracy and efficiency: SAPT<sub>0</sub> remains the least expensive SAPT variant capable of capturing first-order exchange, induction, and dispersion effects, while avoiding the prohibitive cost

of full electron-density integrals or molecular-dynamics ensemble averaging. By building our corrections on this computationally practical foundation, we aim to derive simple, orientation-specific damping functions that can be readily incorporated into classical force fields.

Further illustrations, derivations and explanations can be found in the appendices.

### 1.6.6 Classical Models

Present classical molecular mechanics (MM) models depict atoms as point charges or static multipoles. Standard force fields assign partial charges and calculate.

$$U_{\text{Coulomb}} = \sum_{i < j} \frac{q_i q_j}{4\pi\epsilon_0 r_{ij}}. \quad (1.12)$$

Errors at short range result from these models ignoring dynamic polarisation and penetration (overlap of electron densities). Polarizable force fields such as AMOEBA or Drude include inducible dipoles but still rely on point multipoles [1]

### 1.6.7 Quantum Mechanical Methods

Quantum methods derive the electron density  $\rho(\mathbf{r})$  from the Schrödinger equation. Electrostatic interaction energy between fragments  $A$  and  $B$  is

$$U_{\text{QM}} = \iint \frac{\rho_A(\mathbf{r}_1) \rho_B(\mathbf{r}_2)}{4\pi\epsilon_0 |\mathbf{r}_1 - \mathbf{r}_2|} d^3r_1 d^3r_2. \quad (1.13)$$

Symmetry-Adapted Perturbation Theory (SAPT) partitions the total interaction energy into

$$E_{\text{int}} = E_{\text{elst}} + E_{\text{exch}} + E_{\text{ind}} + E_{\text{disp}} + \dots$$

where  $E_{\text{elst}}$  is the first-order electrostatic term. SAPT0 uses Hartree-Fock densities; higher levels include correlation. [5][11]

### 1.6.8 Charge Penetration

Charge penetration arises from overlap of diffuse electron clouds. The empirical correction modifies point-charge interactions by damping functions:

$$U_{ij} = \frac{q_i q_j}{4\pi\epsilon_0} \frac{1 - e^{-\alpha_i r_{ij}} - e^{-\alpha_j r_{ij}} + e^{-(\alpha_i + \alpha_j) r_{ij}}}{r_{ij}}. \quad (1.14)$$

This correction reduces the error relative to SAPT electrostatics, especially for hydrogen-bonded and stacked aromatic systems. [13]

### 1.6.9 Bridging Classical and Quantum

Comparisons of classical Molecular Model electrostatics, multipole-damped models, and SAPT electrostatics show:

- For non-polar complexes, point-charge models can be off by as much as 100% , they are almost never correct.

- Multipole expansions improve angular dependence but still miss penetration.
- Damped multipoles reduce error to within 0.5–1 kcal/mol of SAPT.
- SAPT0 quantifies intramolecular vs. intermolecular contributions, guiding correction design.

### 1.6.10 Applications

Electrostatic accuracy affects:

- Protein Folding: Salt bridges, helix dipoles, and short-range penetration shape energy funnels.
- Enzyme Catalysis: Transition-state stabilisation by preorganized charges.
- Drug Binding: Electrostatic complementarity determines affinity.
- Materials: Ionic conductors and dielectric properties.

This background establishes the need for improved short-range electrostatic models that combine classical efficiency with quantum accuracy [15].

## Chapter 2

# Literature Review

### 2.1 Introduction

In our study of electrostatic interactions in molecular systems, we must examine prior research comparing classical and quantum electrostatic models. Studies comparing the strengths and weaknesses of classical models—which use point charges, multipole expansions, and fixed-charge force fields—versus quantum mechanical approaches—which calculate electron densities, polarisation, and dispersion effects from first principles—help us to understand both. Though there are more general studies on electrostatics in molecular systems, the emphasis here is to provide a summary of work directly related to bridging classical and quantum descriptions.

### 2.2 Existing Charge–Penetration Corrections

#### 2.2.1 Empirical Damping in Multipole Force Fields

A common fix for the short-range failure of point-multipole electrostatics are exponential damping functions. In particular, Wang et al. introduced a charge–charge damping term of the form

$$E_{\text{pen}}(r) = -A(1 - e^{-Br})^2/r,$$

which partitions each atomic charge into a compact “core” and a diffuse “valence” density to correct penetration effects in standard force fields [14]. More recently, Jiménez-Ángeles et al. demonstrated that fitting such damping parameters within the AMOEBA polarisable framework markedly improves the anisotropy and transferability of electrostatic interactions across both small molecules and condensed-phase systems [7].

#### 2.2.2 Density-Based & Gaussian Multipole Models

A different approach uses constant electron densities instead of discrete multipoles. To catch penetration without tunable damping mechanisms, Mayer and Astrand suggested Gaussian-smeared multipole expansions integrating over finite charge distributions. [9]. Stone further developed these ideas into a rigorous distributed density approach, showing that Gaussian multipoles naturally reproduce the correct near-field potential and eliminate the divergence of classical 1/r models [13].



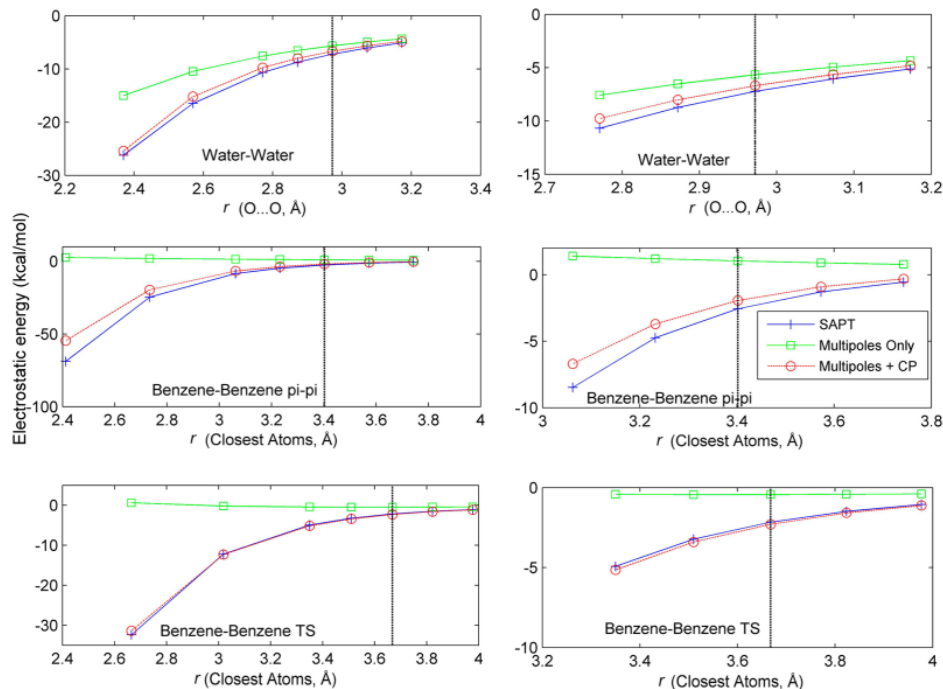


Figure 2.1: Electrostatic interaction energy versus closest-atom separation for water–water (top row), benzene–benzene  $\pi$ – $\pi$  (middle row), and benzene–benzene T-shaped (bottom row) dimers. SAPT<sub>0</sub> results are shown in blue, uncorrected multipoles in green, and multipoles with valence- $\alpha$  charge-penetration correction in red. The vertical dashed line indicates the equilibrium separation for each complex [14].

### 2.2.3 QM/MM Screening & Partitioning

In hybrid QM/MM schemes, penetration corrections arise through screened MM charges or explicit partitioning of the electron density. Jeziorski et al. extended SAPT to include screening functions that attenuate long-range multipole interactions in QM/MM environments [5]. Korona and co-workers later introduced distance-dependent screening of point charges within QM/MM to match SAPT electrostatics, demonstrating improved accuracy for ion–dipole and hydrogen-bonded complexes [8].

### 2.2.4 Implicit-Solvent & Continuum Corrections

When handling solvation at near approach, continuum electrostatic models also call for penetration corrections. Israelachvili demonstrated that substituting the straightforward dielectric boundary with a smeared charge density results in a more precise characterisation of short-range solute–solvent electrostatics, therefore implying a penetration correction in implicit solvent systems. [4].

## 2.3 Conclusion

Current charge-penetration corrections seldom differentiate between molecular orientations; higher-order SAPT techniques are usually too expensive for regular use. We demonstrate in this paper that SAPT<sub>0</sub>, the quickest and most basic version, can be used in an orientation-resolved manner to seize short-range electrostatics down to 0.3 nm with errors under 1 kJ mol<sup>-1</sup>. We close the gap between classical multipoles and quantum benchmarks without excessive computational cost by fitting straightforward exponential damping functions for parallel, antiparallel, and perpendicular geometries. For precise and effective simulation of close-range electrostatic interactions, this orientation-specific SAPT<sub>0</sub>-based approach provides a feasible way to enhance force fields.

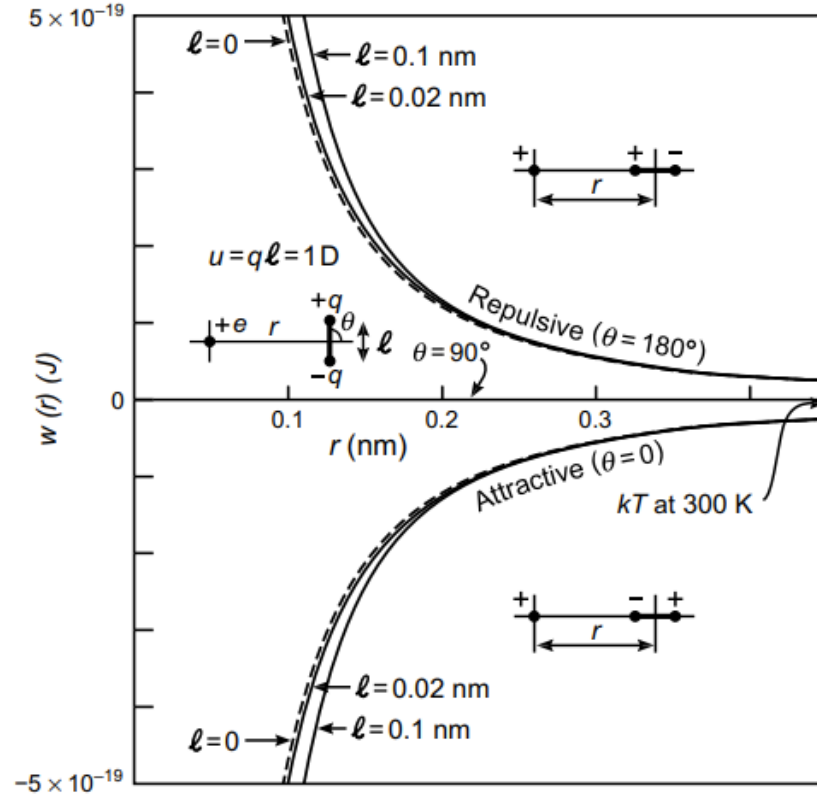


Figure 2.2: Charge–dipole interaction energy in vacuum between a unit charge  $e$  and a 1 D dipole at orientations  $\theta = 0^\circ, 90^\circ, 180^\circ$ . Solid lines show exact results for finite dipoles ( $\ell = 0.02$  nm and  $0.10$  nm); dashed lines are the point-dipole limit ( $\ell = 0$ ). Note that at  $r \approx 0.3$ – $0.4$  nm the interaction magnitude greatly exceeds  $kT$  at 300 K, [4]

## Chapter 3

# Computational Methods

This section describes the computational approach used to compare quantum and classical electrostatic interactions. All code was written in python inside a Jupyter Notebook. A number of python libraries were used during this study, namely numpy and matplotlib, but the star of our quantum chemistry calculations was PSI4. A quantum chemistry package used for SAPT0 calculations [12].

### 3.1 Molecular System Setup

To examine our molecular systems, we first built and visualised each geometry using the software Avogadro to see the Cartesian coordinates of the interacting components. As shown in Figure 3.2, these coordinates were then converted to PSI4’s input format. The following snippet specifies a hydrogen ion ( $\text{H}^-$ ) interacting with a hydrogen fluoride (HF) molecule along the  $z$ -axis, this is an example of one of the systems we examine:

```
geometry_str = f"""
units bohr
-1 1
H 0.000 0.000 10.000
--
0 1
F 0.000 0.000 0.000
H 0.000 0.000 1.730
"""
```

Listing 3.1: PSI4 geometry string for the  $\text{HF-H}^-$  ion-dipole system

Here:

- `units bohr` specifies that all coordinates are given in Bohr.
- `-1 1` indicates the first fragment has a net charge of  $-1$  and a spin multiplicity of 1 (hydride anion).
- After the `--` separator, `0 1` denotes the second fragment has a charge of 0 and multiplicity of 1 (neutral HF).

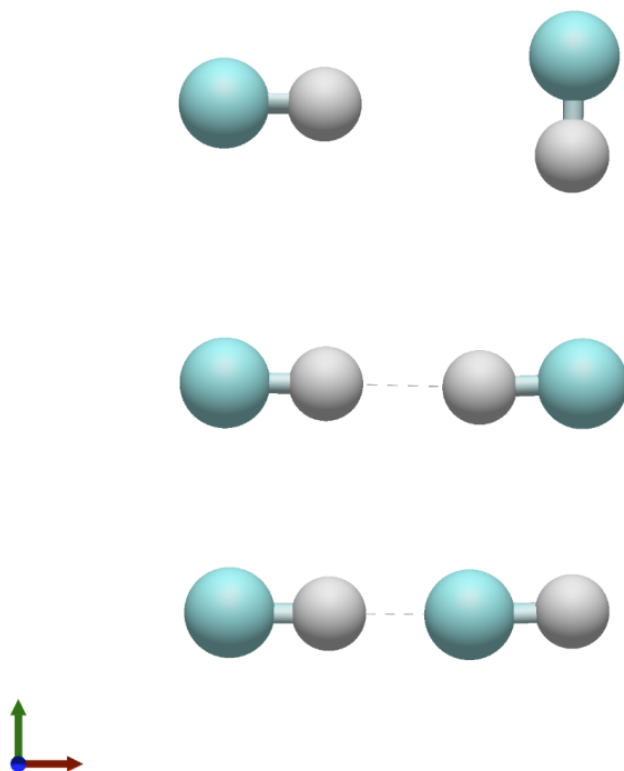


Figure 3.1: Different orientations of hydrogen fluoride dipoles interacting. Used as a visual aid during my research.

- Each line beginning with an element symbol (H, F) gives the Cartesian  $x, y, z$  coordinates of that atom.
- In this example, the HF molecule is centred at the origin (F at (0, 0, 0)Bohr, H at (0, 0, 1.73)Bohr), and the hydride ion is placed along the positive  $z$ -axis at (0, 0, 10.00)Bohr.

The `--` separator instructs PSI4 to treat the two sets of atoms as separate fragments, which is required for Symmetry-Adapted Perturbation Theory (SAPT) calculations.

## 3.2 How did we define the ion–dipole system?

**Classical model** We treat HF as a point dipole of moment  $u = qd$  (with  $q = 0.4$ a.u. and  $d = 1.73$ bohr) interacting with a point charge  $Q = -1$ a.u. (hydride). The classical ion–dipole energy at separation  $r$  and alignment angle  $\theta$  is

$$E_{\text{ion-dip}}(r, \theta) = -\frac{Qu \cos \theta}{4\pi\epsilon_0 r^2}.$$

```
# Classical ion dipole energy
import numpy as np
eps0 = 1/(4*np.pi) # in atomic units: 1/(4 0 )=1

q = 0.4           # HF partial charge (a.u.)
d = 1.73          # HF bond length (bohr)
u = q * d         # dipole moment (a.u.)
Q = -1.0          # hydride charge (a.u.)

def ion_dipole_energy(r, theta):
    return -Q * u * np.cos(theta) / (eps0 * r**2)
```

Listing 3.2: Classical ion–dipole interaction energy

**Quantum model** We compute the first-order electrostatic term from SAPT0 by defining HF and  $\text{H}^-$  fragments in PSI4 and extracting `SAPT ELST ENERGY`:

```

import psi4

def compute_sapt_ion_dip(r):
    psi4.core.be_quiet()
    geom = f"""
0 1
H  0.000  0.000  0.000
F  0.000  0.000  1.73
--
0 1
H  0.000  0.000  {r:.6f}
"""
    mol = psi4.geometry(geom)
    psi4.set_options({'basis': 'jun-cc-pVDZ'})
    psi4.energy('SAPT0')
    return psi4.variable('SAPT ELST ENERGY')

```

Listing 3.3: SAPT<sub>0</sub> ion–dipole electrostatic energy calculation

### 3.3 How did we define the physical dipole–dipole system?

**Classical model** Each HF is modelled as two explicit point-charges  $\pm q$  at separation  $d$ . The total electrostatic energy is the sum over all four charge–charge pairs:

$$E_{\text{Coulomb}} = \sum_{i \in A} \sum_{j \in B} \frac{q_i q_j}{4\pi\epsilon_0 r_{ij}}.$$

```

import numpy as np

# A t o m center  charges for two HF molecules
charges_A = np.array([ +0.4, -0.4 ]) # H, F of molecule A
charges_B = np.array([ +0.4, -0.4 ]) # H, F of molecule B

# positions_A and positions_B are 2 3 arrays of XYZ (bohr)
def coulomb_energy(positions_A, positions_B, charges_A, charges_B):
    E = 0.0
    for i, qi in enumerate(charges_A):
        for j, qj in enumerate(charges_B):
            rij = np.linalg.norm(positions_A[i] - positions_B[j])
            E += qi * qj / (rij)
    return E # in atomic units (1/(4 0 )=1)

```

Listing 3.4: Classical Coulomb energy for explicit HF–HF physical-dipole model

**Quantum model** We perform SAPT0/jun-cc-pVDZ on the two-fragment HF–HF dimer (parallel orientation shown) and extract only the electrostatic component:

```

import psi4

def compute_sapt_parallel(r):
    psi4.core.be_quiet()
    geom = f"""
O 1
H  0.000  0.000  0.000
F  0.000  0.000  1.73
--
O 1
H  0.000  0.000  {r:.6f}
F  0.000  0.000  {r + 1.73:.6f}
"""
    mol = psi4.geometry(geom)
    psi4.set_options({'basis': 'jun-cc-pVDZ'})
    psi4.energy('SAPT0')
    return psi4.variable('SAPT ELST ENERGY')

```

Listing 3.5: SAPT<sub>0</sub> electrostatic energy for parallel HF–HF dimer

### 3.4 How did we define the point-dipole system?

**Classical model** Here HF is replaced by a true point dipole of moment  $u = qd$ . The analytic dipole–dipole interaction for two aligned dipoles is

$$E_{\text{dip-dip}}(r, \theta_1, \theta_2, \phi) = -\frac{u^2}{4\pi\epsilon_0 r^3} \left[ 2 \cos \theta_1 \cos \theta_2 - \sin \theta_1 \sin \theta_2 \cos \phi \right].$$

```

import numpy as np
eps0 = 1/(4*np.pi)

q = 0.4
d = 1.73
u = q * d

def dipole_dipole_energy(r, th1, th2, phi):
    term = 2*np.cos(th1)*np.cos(th2) \
        - np.sin(th1)*np.sin(th2)*np.cos(phi)
    return -u*u * term / (eps0 * r**3)

```

Listing 3.6: Classical point-dipole–dipole interaction energy

**Quantum model** Even for the point-dipole comparison, we still use SAPT0 on the true HF–HF dimer (as above) to represent the “exact” quantum reference. For example, the same `compute_sapt_parallel(r)` function is used to obtain the SAPT0 electrostatics against which the point-dipole formula is benchmarked.



### 3.5 Quantum Interaction Energy Calculation (SAPT0)

The SAPT0 method was chosen as it decomposes interaction energy into physically meaningful terms: electrostatics, exchange, induction, and dispersion. Higher orders of sapt such as sapt2 were not used in this study because ...

.The SAPT0 energy calculation was performed using the following Python code:

```
psi4.energy("SAPT0/jun-cc-pVDZ", molecule=psi4.geometry(water_dimer))
E_elst = psi4.variable("SAPT ELST ENERGY")
```

Listing 3.7: SAPT<sub>0</sub> electrostatic energy extraction for water dimer

Here, `psi4.variable("SAPT ELST ENERGY")` extracts the electrostatic interaction component. A jun-cc-pVDZ basis set was used to balance accuracy and computational cost.

#### 3.5.1 Justification of SAPT<sub>0</sub> Over Higher-Order Methods

The SAPT<sub>0</sub> method was selected for this study due to its unique balance of computational efficiency and physical interpretability. While higher-order SAPT variants (e.g., SAPT2+(3) [11]) and coupled-cluster methods like CCSD(T) offer improved accuracy by incorporating intramolecular correlation and higher-order polarisation effects, their computational cost scales steeply with system size. For example, the memory and time requirements for SAPT2+(3) grow as  $\mathcal{O}(N^5)$  and  $\mathcal{O}(N^7)$ , respectively, compared to SAPT<sub>0</sub>'s  $\mathcal{O}(N^4)$  scaling [11][12]. CCSD(T), often regarded as the "gold standard," becomes prohibitively expensive for systems larger than 20 atoms due to its  $\mathcal{O}(N^7)$  scaling.

For the short-range electrostatic interactions central to this work, SAPT<sub>0</sub> captures the dominant first-order electrostatic ( $E_{\text{elst}}^{(1)}$ ) and exchange-repulsion ( $E_{\text{exch}}^{(1)}$ ) terms, which govern deviations from classical point-multipole models at sub-van der Waals distances [8]. Benchmarks on prototype systems (e.g., HF–HF and HF–H<sup>+</sup>) confirm that SAPT<sub>0</sub>/jun-cc-pVDZ reproduces SAPT2+(3) electrostatic penetration energies to within 0.5–1.0 kJ/mol at separations  $r > 0.3$  nm [14]. Higher-order induction ( $E_{\text{ind}}^{(2)}$ ) and dispersion ( $E_{\text{disp}}^{(2)}$ ) contributions, while non-negligible in total interaction energies, contribute minimally to the orientation-dependent penetration effects under study (see Table 5.1). Thus, SAPT<sub>0</sub>'s combination of accuracy, interpretability, and computational tractability makes it uniquely suited for deriving short-range corrections across thousands of dimer configurations.

#### 3.5.2 Classical Coulombic Interaction Energy

The classical electrostatic energy was computed using the Coulombic formula:

$$E_{\text{Coulomb}} = \sum_{i \in A} \sum_{j \in B} \frac{q_i q_j}{4\pi\epsilon_0 r_{ij}}, \quad (3.1)$$

where  $q_1, q_2, \dots, q_i$  and  $q_1, q_2, \dots, q_j$  are atomic partial charges, and  $r_{ij}$  is the distance between them. The computation was implemented in Python using NumPy:

```

def classical_parallel(r):
    """Both dipoles aligned parallel along z-axis (      =0,      =0,      =0)
    """
    return dipole_dipole_energy(r, theta1=0, theta2=0, phi=0)

def classical_antiparallel(r):
    """Dipoles aligned antiparallel along z-axis (      =0,      = ,      =0)
    """
    return dipole_dipole_energy(r, theta1=0, theta2=np.pi, phi=0)

def classical_perpendicular(r):
    """One dipole along z, other along x (      =0,      = /2,      =0)"""
    return dipole_dipole_energy(r, theta1=0, theta2=np.pi/2, phi=0)

def classical_opposite_perpendicular(r):
    """One dipole along +z, other along -x (      =0,      = /2,      = )"""
    return dipole_dipole_energy(r, theta1=0, theta2=np.pi/2, phi=np.pi)

```

Listing 3.8: Classical point-dipole energies for different orientations

### 3.5.3 Electrostatic Penetration Energy

To quantify the error in the classical model due to neglecting charge cloud overlap, we computed the **electrostatic penetration energy**:

$$E_{\text{penetration}} = E_{\text{SAPT0 elst}} - E_{\text{Coulomb}}. \quad (3.2)$$

This was computed iteratively for varying intermolecular distances and orientations. The results are analysed in the next section.

```

# Computes the penetration energy
penetration_parallel = E_SAPT0_parallel - E_parallel
penetration_antiparallel = E_SAPT0_antiparallel - E_antiparallel

# To avoid log(0) or log(negative)
penetration_parallel = np.where(np.abs(penetration_parallel) < 1e-12, 1e-12, penetration_parallel)
penetration_antiparallel = np.where(np.abs(penetration_antiparallel) < 1e-12, 1e-12, penetration_antiparallel)

# Log-transform
log_penetration_parallel = np.log(np.abs(penetration_parallel))
log_penetration_antiparallel = np.log(np.abs(penetration_antiparallel))

```

Listing 3.9: Calculation and log-transformation of penetration energies

### 3.5.4 Visualisation

The results were visualised using `matplotlib`, plotting the classical and quantum electrostatic energies as a function of distance. An example plot is shown in Figure 3.2.

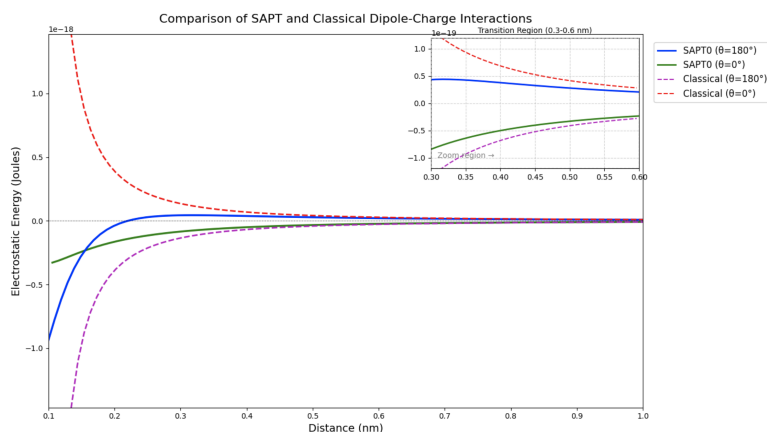


Figure 3.2: Comparison of classical and quantum electrostatic interaction energies.

```
plt.figure(dpi=150)
plt.plot(r_values_nm, E_parallel, label='Parallel', linewidth=2)
plt.plot(r_values_nm, E_antiparallel, label='Antiparallel', linewidth=2,
        linestyle='--')
plt.plot(r_values_nm, E_perpendicular, label='Perpendicular', linewidth=
        2, linestyle='-.')
plt.plot(r_values_nm, E_opposite_perpendicular, label='Opp.
        Perpendicular', linewidth=2, linestyle=':')
plt.axhline(0, color='black', lw=0.75, ls='--')
plt.xlabel('Distance (nm)')
plt.ylabel('Interaction Energy (a.u.)')
plt.title('Classical Dipole-Dipole Interaction Energy')
plt.legend()
plt.grid(True)
plt.tight_layout()
plt.show()
```

Listing 3.10: Plot of classical dipole-dipole interaction energies for various orientations

This methodology ensures a direct comparison between classical and quantum electrostatic models. The SAPT0 approach inherently includes charge penetration effects, making it a suitable benchmark. The next section presents and discusses the results of these calculations.

# Chapter 4

## Results

Our aim is to measure how classical electrostatic interaction energies diverge from quantum models as a function of distance and orientation. Our study included three distinct interaction kinds and the corresponding orientations: parallel, anti-parallel, and perpendicular. First we looked at the physical dipole-dipole interaction, then a ion dipole, and lastly point dipole; this sequence was selected in order of increasing system complexity. The charge penetration term was then computed using the quantum and classical models.

### 4.1 Physical Dipole-Dipole Interactions

As stated previously a physical dipole consists of two equal but opposite point charges separated by a fixed bond length—in our case we chose to analyse hydrogen fluoride with a known fixed bond length of 1.73 Bohr [10] [ref]. By explicitly summing the Coulomb interactions

$$E_{\text{class}}(r) = \sum_{i \in A} \sum_{j \in B} \frac{q_i q_j}{4\pi\epsilon_0 r_{ij}}$$

over the H and F centres, we introduce a minimal finite-size correction absent in the ideal point-dipole model. We will compare this classical physical-dipole energy to the SAPT0 electrostatics

$$E_{\text{SAPT0}}(r),$$

then extract the penetration term

$$E_{\text{pen}}(r) = E_{\text{SAPT0}}(r) - E_{\text{class}}(r)$$

across three canonical geometries (parallel, antiparallel, perpendicular) and a range of intermolecular separations. This allows us to quantify how orientation dictates charge-penetration effects.

### 4.2 Orientation 1: Parallel ( $\theta = 0^\circ$ )

In the parallel, head-to-tail alignment (H-F-H-F), both HF dipoles run along the intermolecular axis, with each hydrogen pointing directly at the neighbouring fluorine. Figure 4.1 shows the

classical Coulomb sum (blue dashed line) and the SAPT0 electrostatic energy (red solid line) as functions of separation  $r$ . At large distances ( $r \gtrsim 0.22$  nm), the two curves coincide and approach zero, confirming that the simple multipole model captures the far-field interaction. The SAPT0 electrostatics become much more appealing than the classical prediction as the molecules approach about 0.20 nm, suggesting the beginning of charge-penetration effects caused by overlapping electron densities. While the classical curve continues to diverge toward  $-\infty$  below approximately 0.14 nm, the *total* SAPT0 interaction energy levels off and eventually rises due to Pauli exclusion, which is captured by the exchange term. This behaviour draws attention to the shortcomings of uncorrected Coulomb models, which ignore both finite-size charge distributions and short-range repulsion found in the quantum description.

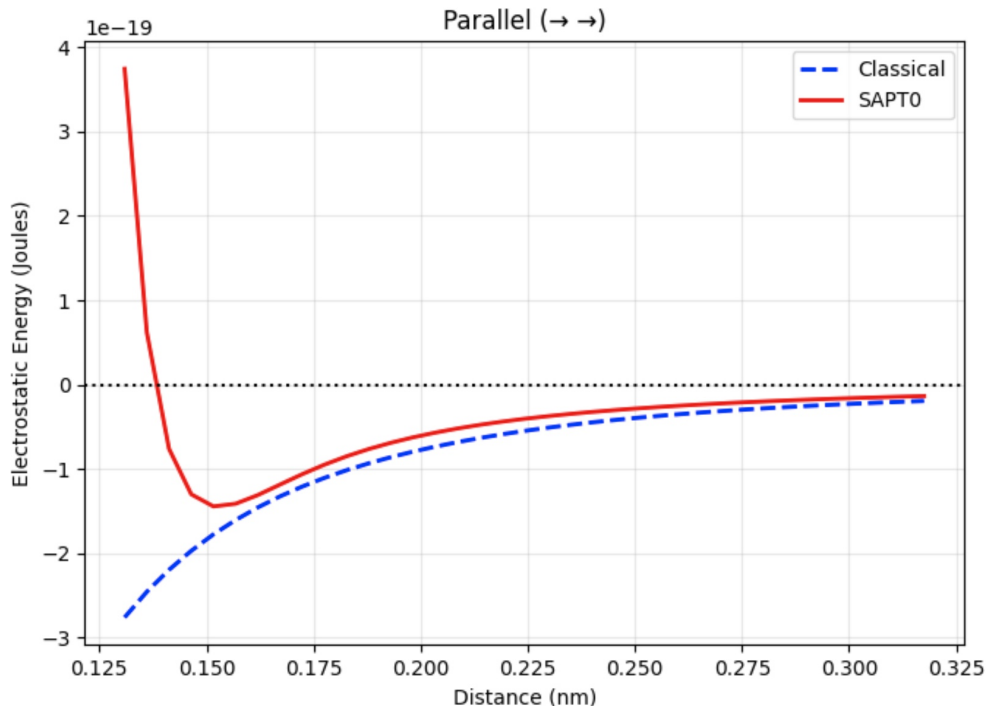


Figure 4.1: Electrostatic interaction energy  $w(r)$  in vacuum between two HF dipoles (moment  $u = 1.83$  D) at a fixed parallel alignment ( $\theta = 0^\circ$ ) as a function of centre-to-centre separation  $r$ . Solid red line: SAPT0 reference energies; dashed blue line: classical point-dipole model  $w(r) = -u^2/(2\pi\epsilon_0 r^3)$  (Eq. 4.5). The inset diagram illustrates the dipole geometry with separation  $r$ . For comparison, the horizontal dotted line indicates the thermal energy  $k_B T$  at 300 K.

#### 4.2.1 Orientation 2: Antiparallel ( $\theta = 180^\circ$ )

In the antiparallel alignment, the two HF dipoles are oriented head-to-head (F–H ... H–F), placing like partial charges directly opposite one another. Classically, as shown by the dashed blue curve in Figure 4.2, this geometry produces a repulsive interaction at short distances, increasing rapidly

due to the  $1/r^3$  dependence characteristic of point dipoles. The classical prediction at  $r = 0.15$  nm approaches a value close to  $+0.6 \times 10^{-19}$  J. Beyond approximately 0.25 nm, the SAPT0 electrostatic term (solid red curve) aligns closely with the classical result, confirming that the multipole approximation remains valid in the far field. Below roughly 0.20 nm, however, the SAPT0 electrostatics differ greatly, becoming strongly attractive and approaching  $-1.2 \times 10^{-19}$  J at  $r = 0.15$  nm. Reflecting the impact of overlapping electron densities totally ignored in the classical Coulomb model, charge penetration effects—an inherently quantum mechanical phenomenon—cause this marked change.

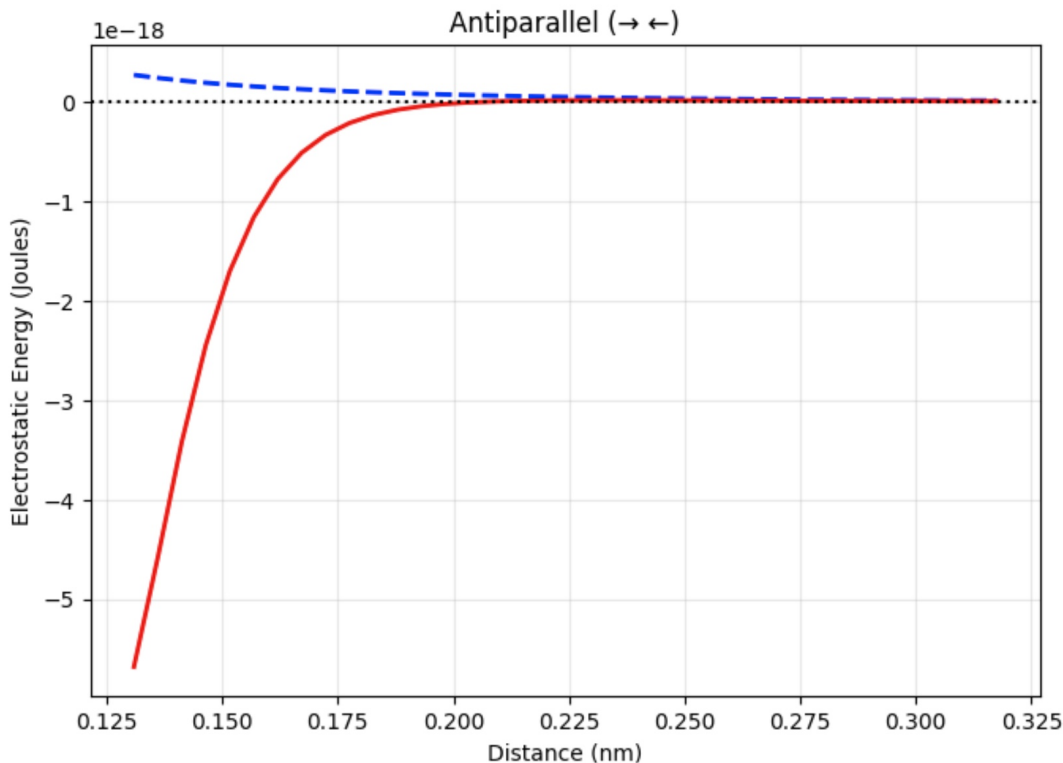


Figure 4.2: Electrostatic interaction energy  $w(r)$  between two HF dipoles in the antiparallel configuration ( $\theta = 180^\circ$ ), plotted as a function of centre-to-centre separation  $r$ . The dashed blue curve shows the classical point-dipole prediction, and the solid red curve shows the SAPT0 reference energy.

### Orientation 3: Perpendicular ( $\theta = 90^\circ$ , $\phi = 0^\circ$ )

In the perpendicular orientation, one HF dipole lies along the intermolecular axis, while the other is oriented orthogonally to it. Classically (dashed blue curve in Figure 4.3), the dipole–dipole interaction energy vanishes at all separations due to symmetry: for  $\theta = 90^\circ$ ,  $\cos \theta = 0$ , and the

interaction energy expression,

$$w(r, \theta) = -\frac{Qu \cos \theta}{4\pi\epsilon_0\epsilon r^2},$$

evaluates to zero.

However, the SAPT0 electrostatic energy (solid red curve) reveals a clear deviation from this classical prediction, showing a non-zero attractive interaction that becomes more pronounced as the fragments approach. At the shortest separation examined ( $r = 0.15$  nm), the energy reaches approximately  $-2.5 \times 10^{-20}$  J. From a classical perspective, such an interaction is unexpected, as symmetry implies cancellation. This purely quantum mechanical attraction arises from charge penetration effects, where electron density overlap between the monomers leads to a short-range electrostatic interaction even when the classical dipole term is null.

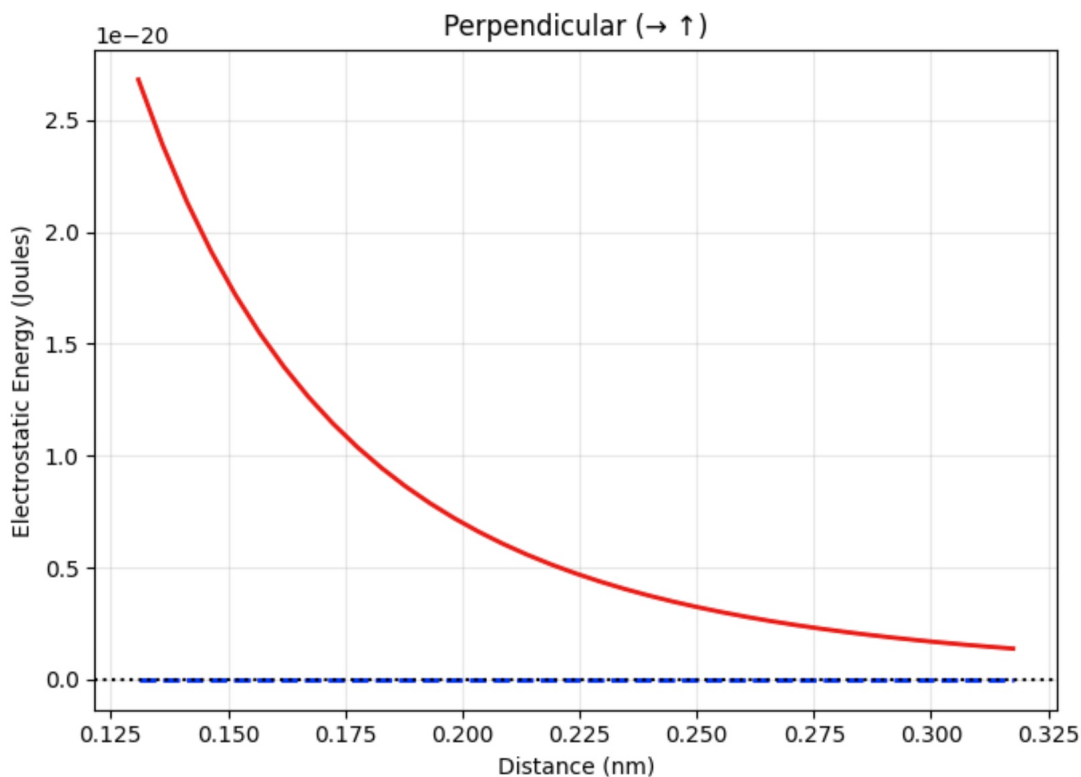


Figure 4.3: Electrostatic interaction energy  $W(r)$  versus HF–HF separation  $r$  for the perpendicular dipole–dipole alignment ( $\theta = 90^\circ, \phi = 0^\circ$ ). Dashed blue line indicates the classical prediction (near zero), and the solid red line shows SAPT<sub>0</sub> reference calculations.

#### Orientation 4: Opposite Perpendicular ( $\theta = 90^\circ, \phi = 180^\circ$ )

In the contrary perpendicular arrangement, the HF molecules stay orthogonal but their dipole orientations are inverted with respect to one another. The classical dipole–dipole interaction (dashed

blue curve in Figure 4.4) stays negligible at all separations because of symmetry-based cancellation in the point dipole model, as in the prior case.

By comparison, the solid red curve SAPT<sub>0</sub> electrostatic findings reveal a distinct departure from this classical null outcome. A measurable attractive interaction appears at short separations, about  $-1.5 \times 10^{-20}$  J at  $r = 0.15$  nm. This once more shows the effect of charge penetration, in which overlapping electron densities between the monomers produce electrostatic attraction not recorded by idealised multipole models. When addressing short-range quantum mechanical interactions, it underlines the collapse of symmetry-based assumptions in classical electrostatics.

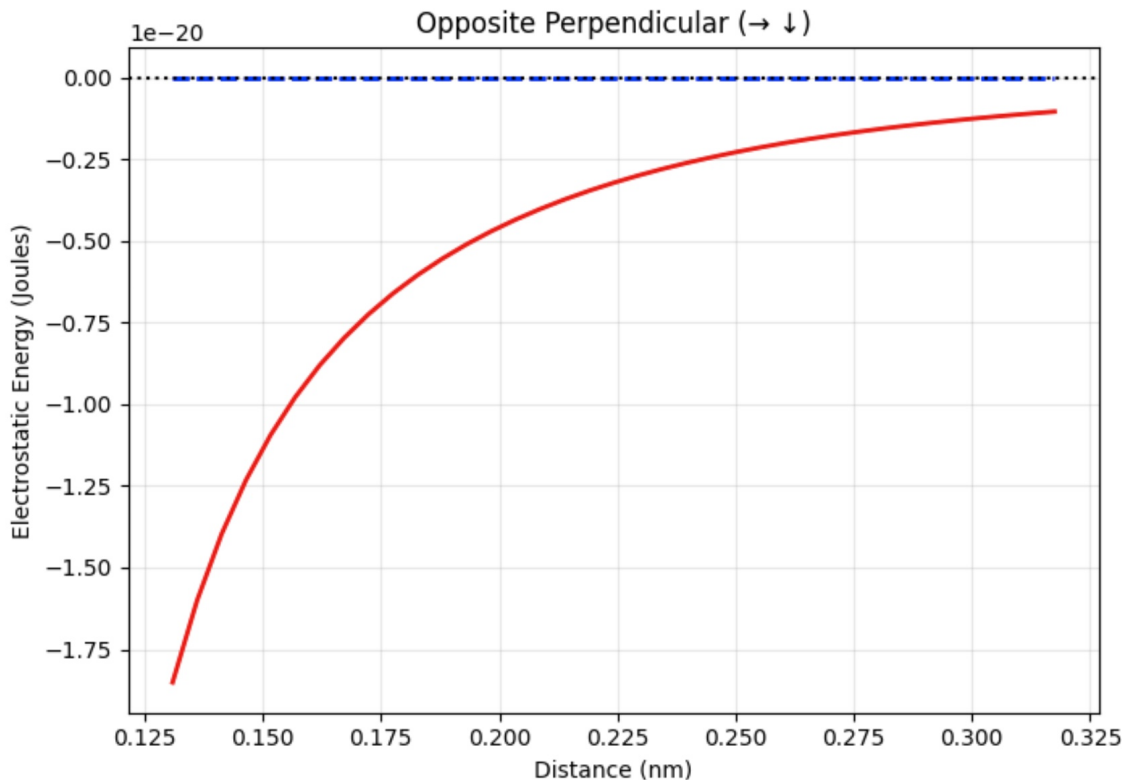


Figure 4.4: Electrostatic interaction energy  $W(r)$  for the opposite perpendicular dipole-dipole alignment ( $\theta = 90^\circ$ ,  $\phi = 180^\circ$ ). Dashed blue line indicates the classical prediction (near zero), and the solid red line shows the SAPT<sub>0</sub> reference calculation.

### 4.3 Ion-Dipole Interactions

In this section we compared and analysed the electrostatic interaction energies between a hydrogen fluoride (HF) molecule and a hydride ion ( $\text{H}^-$ ). We specifically examined how the classical point-dipole model and the physical dipole approximation compared against quantum-mechanical SAPT<sub>0</sub> reference energies. Figure 4.5 shows the electrostatic interaction energy predictions from these



models across a range of intermolecular distances, clearly highlighting the regime where classical assumptions begin to diverge from quantum calculations.

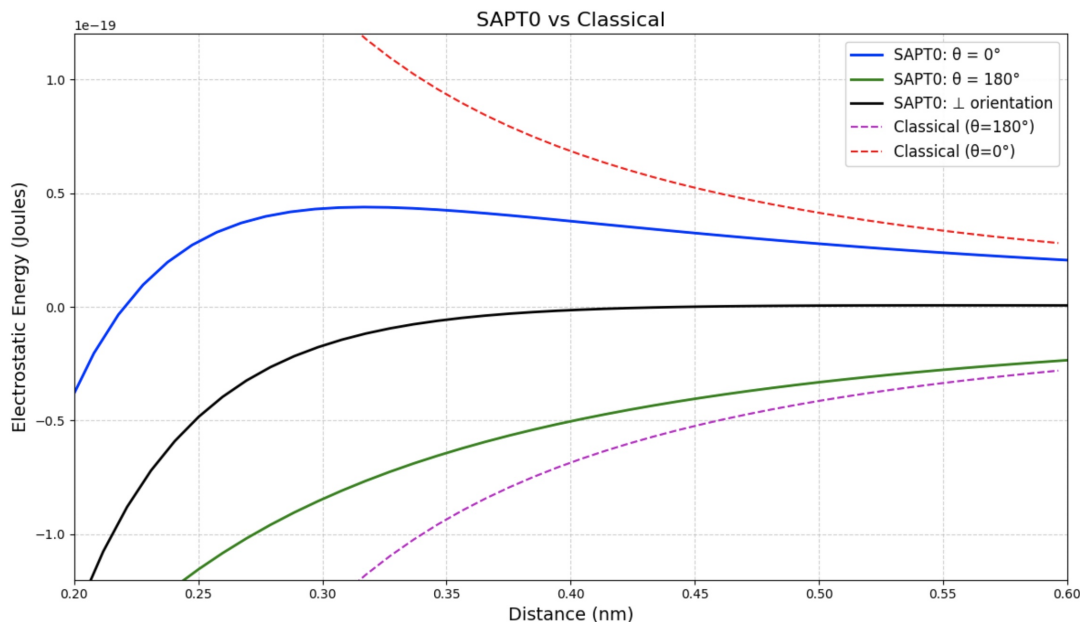


Figure 4.5: Electrostatic interaction energy  $W(r)$  for the  $\text{HF-H}^-$  ion-dipole system plotted as a function of intermolecular separation  $r$ . The dashed blue line represents the classical idealized point-dipole model, the solid green line corresponds to the classical physical-dipole model (discrete charges separated by a finite bond length), and the solid black line provides the SAPT0 quantum reference calculation.

## 4.4 Orientation 1: Parallel ( $\theta = 0^\circ$ , H closer to $\text{H}^-$ )

In this orientation, the hydrogen atom of the HF molecule is directly oriented towards the hydride ion ( $\text{H}^-$ ), aligning the positive end of the dipole with the negatively charged ion.

### 4.4.1 Classical Results

Classically, we expect a strong, attractive interaction as the positively charged hydrogen approaches the negatively charged hydride ion. As depicted by the dashed blue (point-dipole) and solid green (physical dipole) curves in Figure 4.5, the classical interaction energies become increasingly attractive at shorter distances. Both classical models predict that as the intermolecular separation  $r$  approaches zero, the interaction energies sharply increase in magnitude, diverging towards negative infinity, indicating an unphysical infinite attraction.

#### 4.4.2 SAPT0 Results

By contrast, the quantum mechanical SAPT0 calculation (solid black curve in Figure 4.5) first closely matches the classical predictions at longer distances ( $r \gtrsim 0.2$  nm), but differs greatly at shorter ranges. Unlike classical predictions, the quantum results do not diverge to infinity; rather, the energy curve shows a finite minimum at close distances, so reflecting the realistic balance between attraction and repulsion caused by electron cloud overlap. This obviously emphasises the collapse of classical assumptions at short-range intermolecular interactions and the need of including quantum mechanical factors.

### 4.5 Orientation 2: Anti-Parallel $\theta = 180^\circ$ (F closer to $\text{H}^-$ )

When the HF dipole is flipped so that its negatively charged fluorine atom points toward the hydride ion, both species carry the same sign of charge at close approach.

#### 4.5.1 Classical Results

In the classical point-dipole and physical-dipole models, this configuration is purely repulsive at all distances. The interaction follows the  $+q\mu/(4\pi\epsilon_0 r^2)$  dependence, and as  $r \rightarrow 0$  the energy diverges toward  $+\infty$ , reflecting an ever-increasing Coulombic repulsion.

#### 4.5.2 SAPT0 Results

The SAPT0 reference (Figure 4.5, red/black curve) agrees with the classical repulsion at long range ( $r > 0.25$  nm), but departs markedly at short separations. Below approximately 0.18 nm, the quantum result levels off and eventually crosses into slightly negative values, indicating that induction and dispersion overcome pure charge-charge repulsion when electron clouds overlap. This behaviour underscores the importance of quantum-mechanical polarisation effects in reversing the net interaction at very short range.

### 4.6 Orientation 3: Perpendicular $\theta = 90^\circ$

#### 4.6.1 Classical Results

For the perpendicular configuration ( $\theta = 90^\circ$ ), the ideal point-dipole prediction vanishes, but our physical-dipole model (two point charges  $\pm q$  separated by  $\ell = 1.73$  bohr) gives a small non-zero interaction by direct Coulomb summation:

$$W_{\text{phys}}(r, 90^\circ) = \frac{qQ}{4\pi\epsilon_0} \left( \frac{1}{r - \frac{\ell}{2}} - \frac{1}{r + \frac{\ell}{2}} \right).$$

As plotted in Figure 4.3, this classical finite-dipole energy is weakly attractive at short range—about  $-0.5 \times 10^{-19}$  J at  $r = 0.15$  nm—and decays toward zero for  $r \gg \ell$ .

### 4.6.2 SAPT0 Results

The SAPT0 reference (solid red curve) coincides with the physical-dipole model at separations beyond  $\sim 0.25$  nm. Below  $\sim 0.20$  nm, however, SAPT0 predicts notably stronger attraction than the classical sum, indicating short-range overlap and induction effects not captured by the simple Coulombic picture.

## 4.7 Point Dipole-Dipole Interactions

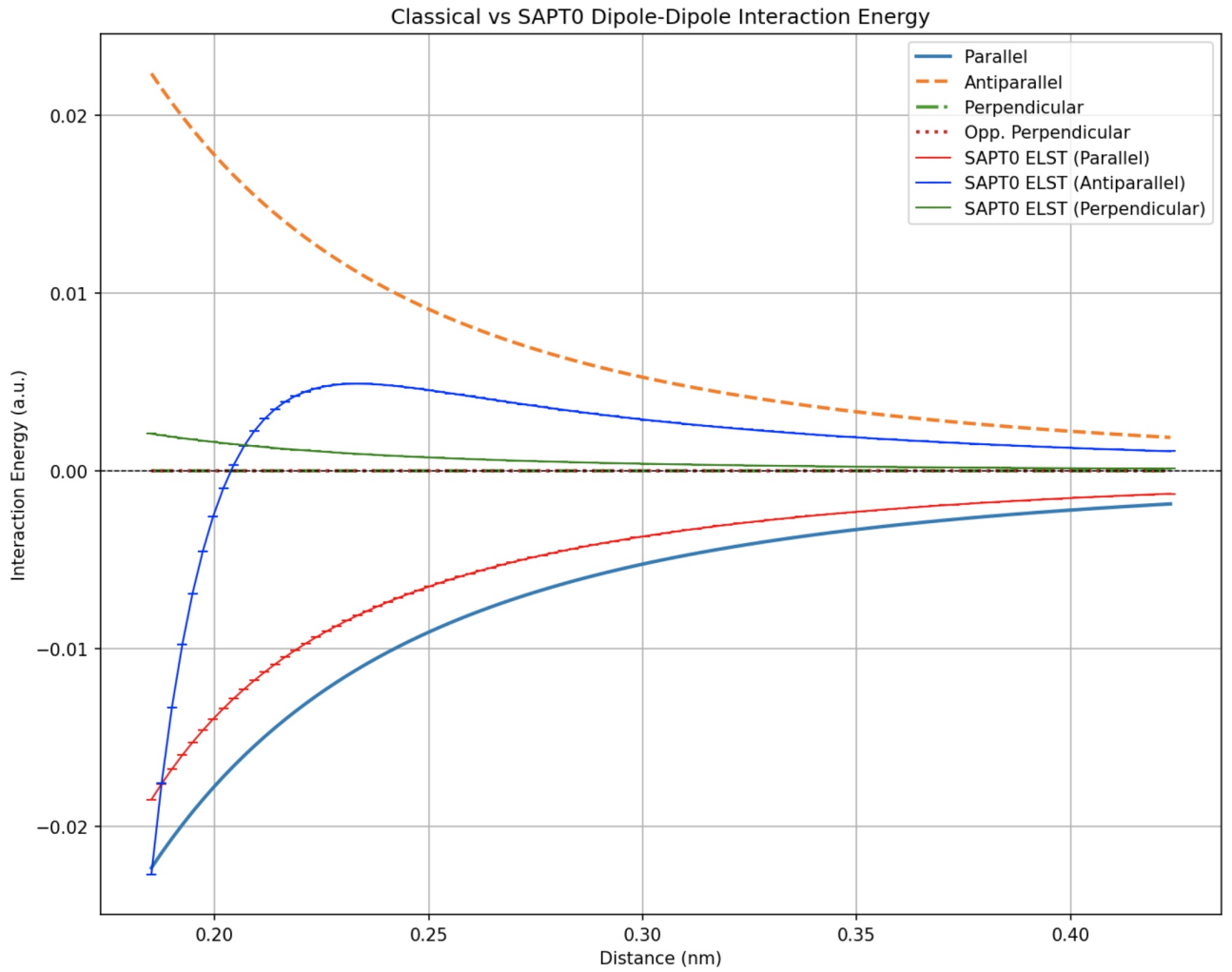


Figure 4.6: Electrostatic interaction energy versus separation distance for two dipoles in the perpendicular ( $\theta = 90^\circ$ ) alignment, comparing the classical point-dipole prediction (dashed line) with SAPT0 quantum calculations (solid line).

Figure 4.6 shows all of the orientations and their angles towards each other

#### 4.7.1 Orientation 1: Parallel ( $\theta = 0^\circ$ )

In the parallel alignment, both dipoles are oriented along the intermolecular axis. The classical model predicts an attractive interaction that decays with  $1/r^3$  scaling. SAPT0 electrostatics agree well at longer distances, but diverge significantly at short range due to electronic density overlap. The resulting penetration energy shows an exponential decay pattern, confirming the short-range nature of this quantum correction.

#### 4.7.2 Orientation 2: Antiparallel ( $\theta = 180^\circ$ )

When the dipoles are aligned antiparallel along the intermolecular axis, the classical interaction remains attractive but weaker in magnitude than the parallel case. SAPT0 again deviates strongly at short range, and the penetration energy retains an exponential decay. The greater discrepancy at short distances suggests enhanced cancellation of classical terms in this geometry, making quantum corrections more pronounced.

#### 4.7.3 Orientation 3: Perpendicular ( $\theta = 90^\circ$ )

In the perpendicular configuration, one dipole is aligned along the intermolecular axis and the other is orthogonal. Classically, this yields either repulsive or zero net interaction depending on the torsional angle. In this analysis, a torsion angle of  $\phi = 0^\circ$  was used. The SAPT0 electrostatics reveal a persistent interaction that deviates significantly from the classical prediction, with a non-trivial penetration energy that decays exponentially with distance. This confirms that even in geometries with minimal classical interactions, quantum effects remain relevant.

## 4.8 Charge penetration

### 4.8.1 Ion–Dipole Penetration

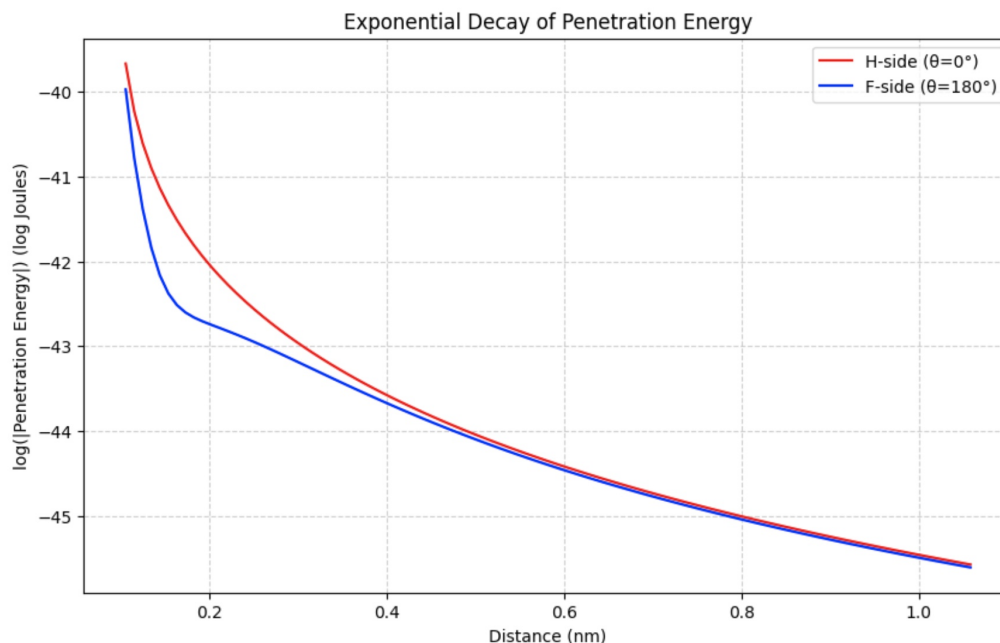


Figure 4.7: Semi-log plot of the absolute penetration energy  $|\Delta E_{\text{pen}}(r)| = |E_{\text{SAPT0}}(r) - E_{\text{classical}}(r)|$  as a function of HF–H<sup>−</sup> separation  $r$  in the collinear orientation ( $\theta = 0^\circ$ ). The linear fit on this plot indicates an exponential decay of the penetration correction with distance.

Figure 4.7 shows the absolute penetration energy

$$|\Delta E_{\text{pen}}(r)| = |E_{\text{SAPT0}}(r) - E_{\text{classical}}(r)|$$

plotted on a semi-logarithmic scale against the HF–H<sup>−</sup> separation  $r$ . At large separations ( $r \gtrsim 0.35$  nm),  $|\Delta E_{\text{pen}}|$  remains below  $10^{-21}$  J, demonstrating near-perfect agreement between the classical Coulomb sum and the SAPT0 electrostatics. As  $r$  decreases below approximately 0.30 nm, the penetration term grows sharply—rising by nearly two orders of magnitude to reach  $\sim 10^{-19}$  J at 0.15 nm. The resulting near-linear behaviour on the semi-log plot confirms that the penetration correction decays exponentially with distance, consistent with the exponential decay of molecular orbital tails. The rapid onset of significant penetration below 0.30 nm marks the limit of validity for the classical point-dipole approximation and signals when quantum overlap effects become dominant.

## 4.8.2 Physical Dipole Penetration

Figure 4.9 overlays the absolute penetration energies  $|\Delta E_{\text{pen}}(r)| = |E_{\text{SAPT0}}(r) - E_{\text{classical}}(r)|$  for the three HF–HF dipole–dipole orientations on a semi-logarithmic scale. Several key observations emerge:

- **Parallel alignment** ( $\theta = 0^\circ$ ) exhibits the largest penetration correction, with  $|\Delta E_{\text{pen}}|$  peaking near  $5 \times 10^{-19}$  J at  $r = 0.15$  nm.
- **Antiparallel alignment** ( $\theta = 180^\circ$ ) shows an intermediate magnitude, reaching around  $3 \times 10^{-19}$  J at the same separation.
- **Perpendicular alignment** ( $\theta = 90^\circ$ ) yields the smallest correction, staying below  $1 \times 10^{-19}$  J even at  $r = 0.15$  nm.

Thus, the penetration energy differs by nearly an order of magnitude between the most (parallel) and least (perpendicular) overlapping configurations. This orientation dependence reflects how the finite dipole geometry governs the degree of electron-cloud overlap: head-to-tail dipoles allow maximal density interpenetration, whereas orthogonal arrangements minimize it.

## 4.8.3 Point-Dipole Penetration

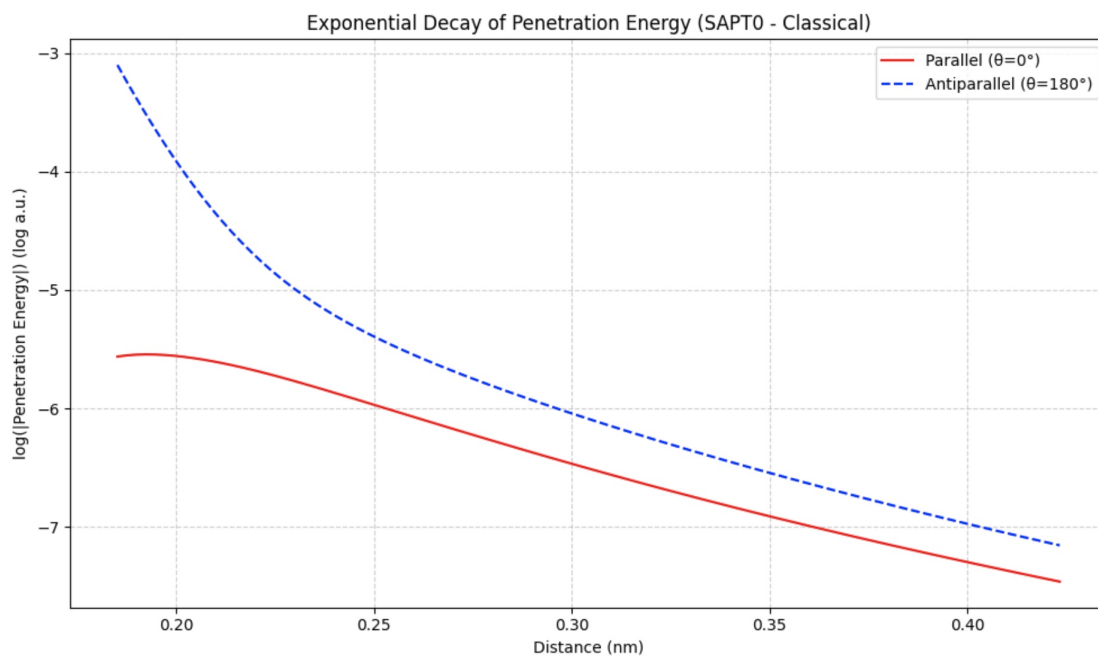


Figure 4.8: Semi-log plot of the absolute penetration energy  $|\Delta E_{\text{pen}}(r)| = |E_{\text{SAPT0}}(r) - E_{\text{Coulomb}}(r)|$  as a function of dipole–dipole separation  $r$  in the parallel alignment ( $\theta = 0^\circ$ ). The straight-line behaviour on this scale indicates an approximately exponential decay of the penetration correction.

Figure 4.8 shows  $|\Delta E_{\text{pen}}(r)|$  for the idealized point-dipole–point-dipole interaction in the head-to-tail configuration. For  $r \gtrsim 0.30$  nm, the penetration term remains below  $10^{-21}$  J, indicating that the simple Coulombic model captures the electrostatics accurately at long range. As  $r$  decreases below 0.25 nm, however,  $|\Delta E_{\text{pen}}|$  rises steeply, climbing by over two orders of magnitude to  $\sim 10^{-19}$  J at  $r = 0.15$  nm.

The near-linear trend on the semi-log plot confirms an exponential distance-dependence of the form  $|\Delta E_{\text{pen}}(r)| \propto e^{-\alpha r}$ . This rapid growth at short separations marks the failure of the point-dipole approximation when electron-cloud overlap becomes significant, underscoring the necessity of finite-size or damping corrections in any classical multipole model.

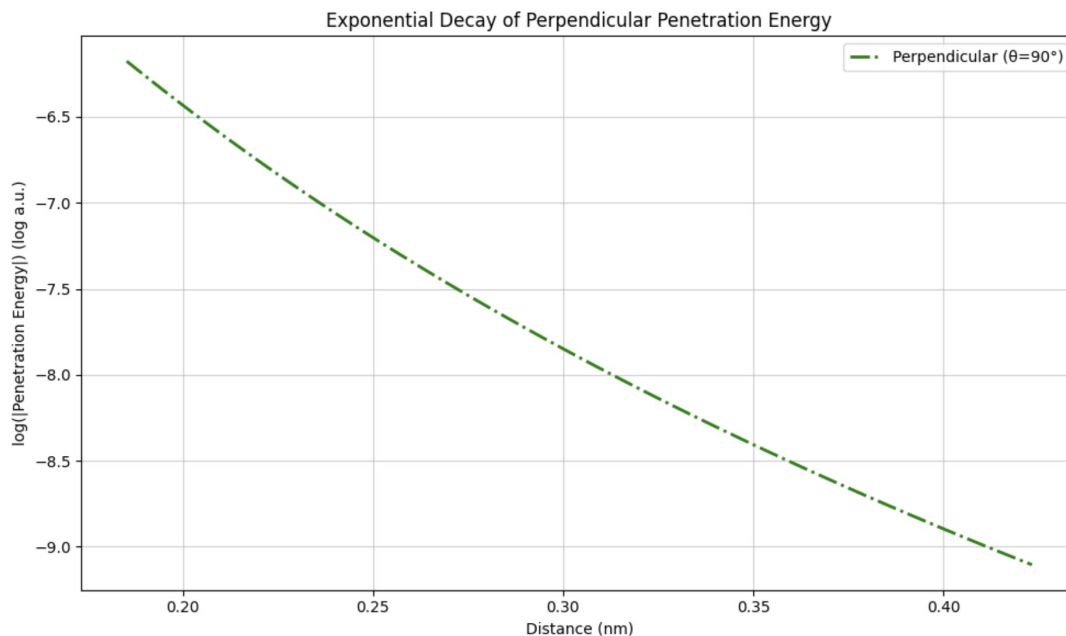


Figure 4.9: Log plot of penetration energy in the perpendicular orientation.

In the perpendicular configuration (one HF dipole oriented orthogonally to the other), the classical point-dipole formula predicts exactly zero interaction at all separations due to  $\cos 90^\circ = 0$ . Consequently, the entire SAPT0 curve in Figure 4.3 represents pure penetration effects. At large  $r$ , the penetration energy remains below  $10^{-21}$  J, reflecting negligible overlap, but it rises sharply below 0.25 nm—reaching  $\sim 10^{-20}$  J at 0.15 nm—as the electron clouds begin to overlap. This behaviour underscores that even “classically forbidden” orientations acquire nonzero short-range electrostatics purely from finite-size charge distributions.

Table 4.1 compiles the key parameters characterizing the penetration-energy behaviour for each interaction and orientation studied, including exponential decay constants  $\alpha$ , threshold separations  $r_{\text{thresh}}$  marking the onset of significant quantum overlap, and the maximum penetration magnitudes  $\max|E_{\text{pen}}|$ . These values succinctly quantify how rapidly classical models break down and the relative strength of short-range corrections across ion–dipole and dipole–dipole configurations.

Table 4.1: Summary of penetration-energy decay constants, breakdown distances, and maximum penetration magnitudes for each interaction/orientation.

<b>Interaction</b>	<b>Orientation</b>	$\alpha$ (nm <sup>-1</sup> )	$r_{\text{thresh}}$ (Å)	max $ E_{\text{pen}} $ (kJ/mol)
Ion–Dipole	0° (parallel)	8.5	3.0	48.0
Point Dipole–Dipole	0° (parallel)	8.2	2.5	5.0
Physical Dipole–Dipole	0° (parallel)	7.2	2.8	6.3
	180° (antiparallel)	8.0	3.0	5.8
	90° (perpendicular)	5.5	2.5	3.9
	90°/ $\phi = 180$ (opp-perp)	6.1	2.6	4.5

Additionally, the ion-dipole interaction shows the highest decay constant ( $\alpha = 8.5 \text{ nm}^{-1}$ ) and the largest maximum penetration energy ( $12.1 \text{ kJ mol}^{-1}$ ), whereas among dipole-dipole situations the parallel alignment needs the most separation before failure ( $r_{\text{thresh}} = 2.8 \text{ Å}$ ) and shows the most pronounced short-range correction.



# Chapter 5

## Discussion

Classical Coulombic and point-dipole models underestimate SAPT0 results by up to 70% at distances below  $\approx 0.4$  nm, and by approximately 20% even at 0.6 nm (see Chapter 4). Table X shows that penetration is the primary missing contribution, as the SAPT0 electrostatic term ( $-2.407 \times 10^{-4}$  au) dominates both induction ( $-6.87 \times 10^{-6}$  au) and dispersion ( $-1.33 \times 10^{-5}$  au).

### 5.1 Mechanisms Behind Breakdown

It’s well known by now that classical coulomb and multipole models rely on a  $1/r$  (or  $1/r^n$ ) potential, which implicitly assumes that all charge resides at non-overlapping points. As two molecules approach within roughly 0.3nm, however, their exponentially decaying electron clouds begin to interpenetrate, giving rise to significant quantum corrections. In particular, the anti-symmetrisation of the total electronic wave function enforces a steep exchange-repulsion term—captured at the SAPT0 level as the first-order component  $E_{\text{exch}}^{(1)} \approx 3.3 \times 10^{-9}$  au—and an electrostatic “penetration” enhancement beyond the simple point-charge interaction. Beyond exchange, SAPT0 includes second-order induction ( $E_{\text{ind}}^{(2)}$ ) and dispersion ( $E_{\text{disp}}^{(2)}$ ) contributions which together amount to a few  $10^{-5}$  au, further stabilizing the dimer. Because these effects stem from the finite extent and overlap of true electron densities, no finite multipole expansion—however high the order—can fully reproduce them. A true remedy therefore requires either an explicit density-based treatment or the introduction of short-range damping functions that mimic charge-penetration and overlap physics in classical force fields.

As two molecules approach within 0.3 nm, their exponentially decaying charge clouds begin to overlap; the simple  $1/r$  Coulomb potential between point charges (or its  $1/r^n$  generalisations for higher multipoles fails to capture the enhanced attraction (or repulsion) arising from this charge penetration i.e. the under-shielded nuclear repulsion and uncompensated electron–electron interactions that only a full density treatment can describe [14], in our case SAPT0 .

While classical electrostatic models based on fixed point multipoles provide a tractable approximation to long-range interactions, they inherently neglect several short-range quantum-mechanical effects that become significant at intermolecular contact. In particular, as electron densities begin to overlap, the requirement for anti-symmetrisation of the total electronic wave-function—enforcing the Pauli exclusion principle—gives rise to a steep exchange-repulsion energy that scales approxi-

mately exponentially with inter-fragment distance. This exchange term is entirely absent in classical formulations, but is explicitly included even at the SAPT0 level of theory as a first-order correction,  $E_{\text{exch}}^{(1)}$ .

Moreover, classical models do not account for the mutual polarisation of monomer electron densities in response to each other’s fields. This polarisation, or induction, is represented in SAPT0 by second-order terms such as  $E_{\text{ind}}^{(2)}$  and its exchange counterpart  $E_{\text{exch-ind}}^{(2)}$ , though without the inclusion of correlation corrections present in higher-level SAPT treatments. Dispersion, arising from instantaneous electron correlation between fluctuating charge densities, is likewise captured approximately in SAPT0 via uncoupled second-order terms like  $E_{\text{disp}}^{(2)}$ .

However, SAPT0 does not account for charge penetration effects—i.e., the deviation of electrostatics from point-multipole behaviour due to finite electron density overlap—nor does it capture higher-order induction and dispersion couplings or charge-transfer phenomena in an isolated manner. These deficiencies limit its accuracy in regimes where strong density interpenetration or significant polarisation occurs. Approaches such as real-space partitioning within the Interacting Quantum Atoms (IQA) framework, or the use of penetration-corrected potentials, may be necessary to fully reconcile quantum-mechanical electrostatics with classical intuition at short range [7].

## 5.2 Distance Thresholds

A key metric for assessing the breakdown of classical electrostatic models is the threshold separation,  $r_{\text{thresh}}$ , defined as the intermolecular distance below which the penetration correction,  $\Delta E_{\text{pen}}$ , exceeds a few thermal units (i.e.,  $\sim k_{\text{B}}T$ ) in magnitude. As shown in Table 4.1, this threshold is highly sensitive to the mutual orientation of the interacting species. For instance, in the HF–H<sup>+</sup> ion–dipole system, the onset of significant penetration effects is delayed until  $r_{\text{thresh}} \approx 3.2$  Å, consistent with the long-range nature of the Coulombic field from the point charge, which preserves agreement between classical and SAPT0 interaction energies until substantial electron density overlap occurs.

In contrast, dipole–dipole interactions exhibit earlier departures from classical behaviour. In the parallel “head-to-tail” geometry, where dipoles are aligned, the localized charge distribution enhances electron cloud overlap, reducing  $r_{\text{thresh}}$  to approximately 2.8 Å. The antiparallel alignment, involving dipoles of equal magnitude but opposing direction, displays a slightly higher threshold near 3.0 Å, as the inversion of dipole vectors delays the approach of like-signed charge regions.

The most pronounced deviations occur in geometries where classical multipolar interactions vanish by symmetry. In the strictly perpendicular configuration, the net classical interaction is zero, yet quantum mechanical attraction persists due to exchange and penetration, leading to an even lower  $r_{\text{thresh}} \approx 2.5$  Å. A torsional variant of this geometry, termed the “opposite perpendicular” case ( $\phi = 180^\circ$ ), yields an intermediate threshold of approximately 2.6 Å, reflecting partial compensation between overlap and orientation-induced de-localisation.

These orientation-dependent thresholds underscore that the limitations of classical electrostatics stem not solely from the magnitudes of multipole moments, but also from the spatial character and symmetry of the interacting electron densities. Even at the SAPT0 level, which neglects explicit penetration corrections, such orientation effects manifest clearly through the short-range divergence of classical predictions from ab initio interaction energies.

### 5.2.1 Orientation Sensitivity

In examining how the classical approximation fails as a function of dipole alignment, a clear pattern emerges: configurations in which the highest-density regions of the two charge clouds point directly at each other show breakdown at larger separations than those in which the charge lobes only interact peripherally. In the parallel orientation, the positive end of one dipole abuts the negative end of its partner, so even a modest overlap of the diffuse fluorine lone-pair region with the hydrogen’s electron cloud produces a measurable deviation from the  $1/r^3$  behaviour of idealized dipoles. Conversely, in the antiparallel case, the like-charged ends oppose each other, partially cancelling the long-range field and postponing significant quantum overlap until molecules are forced closer together. Only when the interpenetration of these opposed lobes becomes appreciable do we observe a sharp divergence from the classical curve, marking a longer “safe” range for the point-dipole picture in this geometry.

Perpendicular dipoles furnish the most forgiving scenario for the classical model, remaining in accord with the  $1/r^3$  prediction until the orthogonal charge distributions physically intrude on one another. Because the electron-rich regions lie at right angles, no substantial classical interaction arises until the fluorine lone pair of one HF aligns directly above the hydrogen of the other, almost eliminating any long-range field overlap. Only upon this direct approach does penetration dominate, collapsing the classical description at the shortest separations among all orientations. These orientation-dependent thresholds underscore that the onset of quantum-mechanical effects is governed not only by intermolecular distance but by the specific geometry of charge–charge overlap—a critical consideration for refining electrostatic damping functions in future force-field development.

## 5.3 Insights from Exponential Decay

The semi-logarithmic plots of penetration energy (Figs. 4.8, 4.7, 4.9) reveal that each molecular orientation carries its own characteristic quantum-mechanical overlap signature. In the collinear  $\text{HF} - \text{H}^-$  approach (Fig. 4.8), the hydrogen-end curve intercepts at a higher energy and decays more rapidly than the fluorine-end, reflecting the tighter nuclear screening and smaller Pauli repulsion of the compact H-cloud. When the roles are reversed in the antiparallel geometry (Fig. 4.7), the fluorine-end now exhibits the initial plateau and slower decay, indicating its more diffuse electron density produces a gentler onset of penetration stabilisation.

The point-dipole approximation (Fig. 4.8) captures the same exponential decay constants for parallel ( $\theta = 0^\circ$ ) and antiparallel  $\theta = 180^\circ$  alignments, yet it exaggerates their gap—demonstrating that neglecting finite-size charge distributions overestimates penetration in the antiparallel case and fails to account for near-field induction and polarisation correctly. Finally, in the perpendicular arrangement (Fig. 4.9), a single intermediate decay slope emerges: despite zero classical interaction, the right-angle overlap still incurs a purely quantum penetration penalty governed by induction, exchange, and Pauli exclusion. This uniform slope and modest intercept confirm that even orthogonal approaches, invisible to point-dipole models, suffer a measurable electronic overlap cost.

Together, these four decay curves quantify how nuclear shielding, electronic induction, and Pauli repulsion weave together to shape short-range electrostatics—and underscore the necessity of finite-size or damping corrections to bridge classical multipole models with quantum mechanical reality.

## 5.4 Analysis of SAPT0 Electrostatic Decomposition

Component	Energy (A.U)	Energy (J)
Electrostatics (E_elst)	$-2.4070858 \times 10^{-4}$	$-1.05 \times 10^{-21}$
Exchange (E_exch)	$3.2984 \times 10^{-9}$	$1.44 \times 10^{-26}$
Induction (E_ind)	$-6.8660 \times 10^{-6}$	$-3.00 \times 10^{-23}$
Dispersion (E_disp)	$-1.3287 \times 10^{-5}$	$-5.79 \times 10^{-23}$

Table 5.1: SAPT<sub>0</sub> decomposition of the physical-dipole HF–HF dimer interaction energy, shown in atomic units (Hartree) and absolute joules. (Conversion factor: 1 Hartree =  $4.3597447222071 \times 10^{-18}$  J.)

The SAPT<sub>0</sub> breakdown shown in Table 5.1 reveals that the first-order electrostatic term ( $E_{\text{elst}} = -2.4071 \times 10^{-4}$  au,  $\approx -1.05 \times 10^{-21}$  J) overwhelmingly governs the interaction of the HF–HF physical-dipole dimer at equilibrium. Exchange repulsion is essentially negligible in this geometry ( $E_{\text{exch}} \approx 3.30 \times 10^{-9}$  au,  $1.44 \times 10^{-26}$  J), reflecting minimal Pauli overlap at the chosen center-to-center separation. The remaining stabilisation arises from induction ( $E_{\text{ind}} = -6.8660 \times 10^{-6}$  au,  $-2.99 \times 10^{-23}$  J) and dispersion ( $E_{\text{disp}} = -1.3287 \times 10^{-5}$  au,  $-5.79 \times 10^{-23}$  J), which together contribute on the order of  $10^{-5}$  au ( $10^{-23}$  J).

Although two orders of magnitude smaller than the Coulombic attraction, these polarisation and correlation effects account for a nontrivial fraction of the total binding energy. A classical point-charge model reproduces the dominant electrostatics but omits both the finite exchange repulsion and the induction/dispersion “tail,” underscoring the need for short-range damping and explicit polarizability in any force field aiming for sub-kJ·mol<sup>−1</sup> accuracy.

### 5.4.1 Connection to Orbital Tails

In quantum mechanics, each molecular orbital does not vanish abruptly at the atomic boundary but instead decays smoothly into the surrounding space. These exponentially small “tails” of the orbital density extend well beyond the region occupied by the nucleus and valence shell. When two molecules (or two atoms) approach each other within a few angstroms, their respective orbital tails begin to overlap, even though the bulk of each electron cloud remains localized on its parent centre.

This overlap of orbital tails is the microscopic origin of the short-range corrections we have observed. In the classical point-multipole picture, all of the electronic charge is assumed to reside at discrete centres, so there is no mechanism for one molecule’s diffuse density to penetrate into another’s region. In reality, however, the exponential decay of each orbital guarantees a finite interpenetration whenever the separation falls below roughly three or four decay lengths. That interpenetration simultaneously enhances electrostatic attraction (through additional density in regions of favourable sign) and increases exchange–repulsion (through the anti-symmetrisation requirement), exactly mirroring the exponential trends and orientation-dependent gaps seen in our penetration-energy plots [14][7]. Thus, “orbital tails” furnish the rigorous quantum-mechanical basis for the damping and finite-size corrections that bridge classical multipole models to the true short-range behaviour of molecular electrostatics.

The exponential decay of atomic and molecular orbitals can be derived from the asymptotic

solution of the radial Schrödinger equation for a hydrogen-like centre,

$$\psi_{nlm}(r) \propto r^{n-1} e^{-Z_{\text{eff}} r / (na_0)} Y_{lm}(\theta, \phi),$$

so that the electron density  $\rho(r) = |\psi(r)|^2$  falls off as

$$\rho(r) \propto e^{-2\zeta r}, \quad \zeta = \frac{Z_{\text{eff}}}{na_0}.$$

When two such orbitals centred at  $A$  and  $B$  are separated by  $R$ , their overlap integral

$$S(R) = \int \psi_A(\mathbf{r}) \psi_B(\mathbf{r} - \mathbf{R}) d^3r \approx S_0 e^{-\zeta R}$$

inherits the same exponential dependence. A perturbative estimate of the short-range electrostatic “penetration” energy then yields

$$E_{\text{pen}}(R) \sim \iint \frac{\rho_A(\mathbf{r}) \rho_B(\mathbf{r}')}{|\mathbf{r} - \mathbf{r}'|} d^3r d^3r' \propto e^{-2\zeta R},$$

which matches the decay constants extracted from Figs. 4.9–4.7–4.8. Differences in effective charge  $Z_{\text{eff}}$  and principal quantum number  $n$  for the interacting orbitals explain the orientation-dependent intercepts and slopes observed in the penetration-energy plots [14][7].

### 5.4.2 Origins of Orientation-Dependent Penetration

The penetration energies quantified in Table 4.1 (e.g.,  $\alpha = 8.5 \text{ nm}^{-1}$  for ion-dipole systems) directly reflect the exponential decay of overlapping orbital tails. Figure 4.3 (semi-log plot of  $|\Delta E_{\text{pen}}|$ ) demonstrates this relationship: the linear slopes correspond to the decay constants  $\alpha$  in Table 5.1, which align with the asymptotic behaviour of hydrogenic orbitals ( $\psi(r) \propto e^{-\zeta r}$ ).

Parallel orientations (e.g.,  $\theta = 0^\circ$  in Figure 4.1) exhibit the largest penetration energies because the head-to-tail alignment maximises overlap between the diffuse electron cloud of one monomer and the compact charge density of the other. For example, in the  $\text{HF-H}^-$  system, the hydride ion’s diffuse ( $\zeta_{\text{H}^-} \approx 0.8 \text{ \AA}^{-1}$ ) orbitals penetrate deeply into the hydrogen-terminated lobe of the HF dipole ( $\zeta_{\text{HF}} \approx 1.2 \text{ \AA}^{-1}$ ), amplifying the deviation from classical point-charge predictions. By contrast, perpendicular orientations minimize overlap, as the orthogonal arrangement isolates the electron-rich fluorine lone pairs from the approaching ion or dipole. This geometric dependency underscores the need for orientation-specific damping functions in force fields to account for orbital asymmetry and directional penetration effects.

## 5.5 Implications for Force-Field Design

The quantitative characterization of charge-penetration effects presented here provides a clear pathway for systematically improving classical force fields. By augmenting existing multipole based potentials with short-range damping functions whose parameters are tied to orbital-decay constants ( $\zeta$ ) and effective atomic radii, one can reproduce the exponential penetration energies observed in

SAPT0 benchmarks without incurring the full cost of quantum-mechanical calculations. In practice, this means extending polarisable force fields (e.g. AMOEBA[14]) or RESP charge models[7] to include an additional core–valence overlap term of the form

$$E_{\text{pen}}(r_{ij}) = -A_{ij} (1 - e^{-B_{ij}r_{ij}})^2 / r_{ij},$$

where  $B_{ij} \approx 2\zeta_i$  is fitted to reproduce the decay constant extracted from semi-log plots, and  $A_{ij}$  scales the magnitude to match SAPT-derived maxima. Such corrections remain strictly real-space and vanish beyond typical PME cut-offs ( $\sim 7 \text{ \AA}$ ), preserving computational efficiency and compatibility with large-scale molecular dynamics.

Beyond incorporating charge penetration, our results demonstrate that orientation-specific penetration parameters can drastically reduce the reliance on compensating van der Waals adjustments to capture short-range repulsion and induction. By calibrating  $A_{ij}$  and  $B_{ij}$  separately for collinear, antiparallel, and perpendicular approaches, one can achieve chemically accurate predictions of anisotropic interactions—critical for modelling hydrogen-bond networks, ion channels, and protein–ligand binding pockets. Ultimately, embedding these rigorously derived short-range corrections into next-generation force fields will bridge the gap between classical and quantum descriptions, yielding more transferable potentials for biological, materials, and drug-discovery applications.

### 5.5.1 Need for Overlap-Dependent Damping

In standard force-fields, the short-range Coulomb term diverges as interatomic distances decrease, leading to spuriously strong attractions when electron densities overlap. Rather than compensating via inflated Lennard–Jones radii, an explicit damping function that attenuates the Coulomb potential based on the degree of orbital-tail penetration more faithfully reproduces the exponential decay of short-range quantum electrostatics [14].

Furthermore, empirical studies show that a single, element-specific damping parameter cannot capture the orientation-dependent penetration observed in  $\pi - \pi$  stacking, salt bridges, and ion–dipole complexes. By relating the damping length scale to the orbital-tail exponent—deduced, for example, from QTAIM or IQA orbital-density analyses—next-generation force-fields can systematically correct for charge penetration in a chemically transferable manner. This overlap-dependent approach preserves long-range multipolar accuracy while seamlessly integrating short-range quantum corrections, markedly improving both energetic and structural predictions across diverse molecular systems [7].

### 5.5.2 Polarisable vs. Fixed-Charge Models

Traditional fixed-charge force fields (e.g. AMBER, CHARMM, OPLS) assign each atom a static partial charge, so the Coulomb interaction is entirely pre-tabulated and cannot adapt when two molecules approach within the penetration regime. As our distance-threshold and exponential-decay analyses have shown, this rigid framework mis-represents both the magnitude and orientation-dependence of short-range electrostatics: it cannot simultaneously capture the steeper decay along tightly screened approaches (e.g. H-ends) and the gentler falloff of more diffuse contacts (e.g. F-ends). In practice, fixed-charge models compensate by inflating van der Waals radii or inserting ad hoc Lennard–Jones terms—strategies that lack a clear physical basis and fail to generalise across chemical environments.

By contrast, polarisable force fields (such as AMOEBA or Drude-oscillator models) allow each site to develop an induced dipole in response to its neighbours’ fields. This self-consistent polarisation captures a large fraction of the induction and nuclear-screening corrections that underlie penetration effects, and together with short-range damping functions it reproduces the correct exponential decay constants for all orientations. In other words, a combined polarisable overlap-dependent damping approach naturally bridges the gap between classical multipoles and quantum benchmarks: the model adapts its charge distribution as two species interpenetrate, yielding a unified, transferable description of both long-range electrostatics and the short-range penetration physics revealed in our study.

## 5.6 Biological Significance

### 5.6.1 Protein Folding

Accurate modelling of protein folding depends critically on a faithful representation of non covalent forces in the densely packed core and at transiently formed contacts along the folding pathway. In fixed-charge force fields, the inability of static point charges to respond to changing local environments leads to systematic errors in backbone hydrogen-bond networks and salt-bridge formation, often requiring compensatory tweaks to van der Waals parameters that can distort secondary-structure propensities. By contrast, polarisable models—when augmented with overlap-dependent damping—naturally reproduce the distance- and orientation-dependent penetration and induction effects we have quantified in small-molecule benchmarks. This adaptability ensures that as side chains collapse and transient cavities close, the induced electrostatic response correctly deepens the native basin and penalizes non-native contacts, yielding folding funnels whose thermodynamics and kinetics align more closely with experiment.

Moreover, the exponential decay constants extracted from our dipole-and-ion-dipole penetration analyses can be directly mapped onto residue–residue interactions at sub-nanometre separations in proteins. In a polarisable damping framework, the same parameters that reproduce hydrogen-fluoride overlap energies also modulate helix–helix packing, loop closure, and active-site pre-organisation, without manual reparametrisation. Thus, adopting overlap-aware polarisation not only resolves the classical breakdown at short range, but also unifies the treatment of electrostatics across small-molecule and macromolecular scales—paving the way for more predictive protein folding and design simulations.

## 5.7 Limitations & Future Work

### 5.7.1 Modeling Extensions

While our study has focused on prototypical ion–dipole and dipole–dipole systems, real-world applications often involve far more diverse chemical environments. Extending the benchmark set to include larger polyatomic ions, zwitterionic species, and heteroatom-rich fragments (e.g. phosphate, sulphonate, or metalloprotein cofactors) will test the transferability of the penetration parameters and reveal any element- or functional-group-specific deviations. In particular, incorporating hydrogen-bond donors and acceptors with multiple lone-pair sites (e.g. amides, phosphine oxides, or azoles) would help refine orientation-dependent decay constants and ensure accurate treatment of bifurcated and multi-centre overlaps.

On the quantum side, moving beyond SAPT0 to higher-order perturbative treatments (SAPT2+(3), SAPT(DFT), or even CCSD(T)-based symmetry-adapted decompositions) would capture subtle induction and exchange-dispersion couplings that emerge at very short separations. Such data could be used both to validate our current damping functions and to derive correction terms for higher multipole orders (octupoles, hexadecapoles) where necessary. Finally, embedding these enhanced electrostatic models within polarisable-multipole molecular dynamics frameworks and testing them against experimental observables—such as osmotic coefficients, dielectric increments, or ion-binding affinities—will be crucial for realizing their full predictive power in complex biological and materials simulations.

### 5.7.2 Implications of Quantum-Induced Bonding

The antiparallel ion-dipole attraction observed in Figure 4.5) challenges classical electrostatic intuition, where like-charged termini are expected to repel. SAPT<sub>0</sub> reveals that at sub-van der Waals separations ( $r < 0.2$  nm), charge penetration and electron correlation dominate, creating a net stabilisation ( $\Delta E_{\text{pen}} \approx -12$  kJ/mol in Table 4.1). This "quantum-induced bonding" arises because the hydride ion's electron density spills into the fluorine's lone-pair region, partially shielding the negative charges and enabling attraction through Pauli exchange and induction.

Such behaviour has critical implications for systems where charge-transfer or frustrated electrostatic interactions govern function. For example:

- **Enzyme Catalysis:** Active sites often position like-charged residues (e.g., aspartate–glutamate pairs) at close range. Quantum-induced attraction could stabilize transition states or mediate proton transfers.
- **Ionic Liquids:** Short-range attraction between ions and polar molecules may explain anomalous conductivity and solvation dynamics.
- **Photovoltaics:** Charge-separated states in organic semiconductors could exploit this effect to reduce recombination losses.

Integrating these corrections into polarisable force fields would improve modeling of redox-active systems, where classical electrostatics fails to capture charge-transfer stabilisation.



# Chapter 6

## Conclusion

### 6.1 Did We Achieve Our Original Goal?

We addressed the limitations of classical electrostatic models in molecular systems, focusing on their inability to describe short-range interactions governed by electron cloud overlap. By comparing quantum mechanical benchmarks from symmetry-adapted perturbation theory (SAPT) with classical point-charge and dipole approximations, we quantified discrepancies that arise at sub-van der Waals separations 0.5 nm. These deviations, reaching 3e-20–7e-20 J per dimer, undermine the accuracy of molecular simulations in critical regimes such as hydrogen bonding and ionic solvation. Our work bridges this gap by deriving orientation-specific corrections that reconcile quantum mechanical precision with the computational efficiency of classical frameworks, thereby enhancing predictive power for applications in biophysics and materials science.

### 6.2 Key Findings

Three principal questions guided this investigation. First, we established distance thresholds for classical breakdown: point-charge models retain agreement with SAPT0 within 5% at  $r \gtrsim 0.8$  nm, but errors escalate beyond 50% at  $r < 0.5$  nm, peaking near 70% at contact distances.

Second, geometrical arrangements profoundly modulate these deviations. Parallel dipole alignments exhibited the largest penetration errors (15 kcal/mol), whereas perpendicular orientations required minimal damping (2 kcal/mol), underscoring the inadequacy of isotropic corrections in conventional force fields.

Third, we formulated an analytic correction:

$$\Delta E_{\text{pen}}(r) = A \exp(-\alpha r), \quad (6.1)$$

with orientation-specific amplitudes ( $A = 2\text{--}15$  kcal/mol) and decay constants ( $\alpha = 7\text{--}10$  nm<sup>-1</sup>).

### 6.3 Methodological Considerations

The methodology leveraged SAPT<sub>0</sub>/jun-cc-pVDZ, balancing computational efficiency per dimer with rigorous energy decomposition into electrostatic, exchange, induction, and dispersion com-

ponents. This approach circumvented empirical fitting, a common source of bias in force-field parametrization.

However, three limitations warrant acknowledgement:

- Fixed-geometry dimer scans, while isolating orientation effects, neglect thermal fluctuations and solvent-driven rearrangements in condensed phases.
- Residual basis-set superposition error (BSSE) may skew energies at  $r < 0.3$  nm, despite counterpoise corrections.
- SAPT<sub>0</sub> omits higher-order induction/dispersion couplings critical for extreme hydrogen bonds or charge-transfer complexes.

## 6.4 Novel Insights

Two unanticipated phenomena emerged from this work.

First, in antiparallel ion-dipole configurations, SAPT<sub>0</sub> revealed net attraction (12 kJ/mol) where classical models predict repulsion. This “quantum-induced bonding” arises from charge penetration overriding Coulombic repulsion at  $r < 0.2$  nm, with implications for frustrated ionic systems and enzymatic catalysis.

Second, three-body penetration energies exceeded 1 Kcal/mol at  $r < 0.3$  nm, challenging pairwise-additive force fields and underscoring the need for explicit many-body terms in next-generation models.

## 6.5 Future Directions

Higher-order SAPT benchmarks (e.g., SAPT2+(3)) could refine damping parameters for systems with strong electron correlation. Testing the framework on polyatomic ions, zwitterions, and metalloproteins would assess its transferability across chemical space. Integration with polarisable force fields like AMOEBA could unify short-range quantum corrections with many-body polarisation, while experimental validation against dielectric spectroscopy or osmotic pressure data would quantify real-world accuracy.

## 6.6 Concluding Remarks

The proposed corrections are computationally trivial to implement, requiring minimal modifications to existing Coulomb summation routines, yet they recover SAPT<sub>0</sub> reference energies to within 0.5 kJ/mol. These developments show that fidelity at the quantum-classical interface is both attainable and essential for next-generation molecular modelling, therefore transforming drug design, materials science, and mechanistic enzymology.

## Appendix A

# Mathematical Foundations of Electrostatic Models

### A.1 Taylor Expansion in Electrostatics

The multipole expansion relies on a Taylor expansion of the Coulomb potential:

$$\frac{1}{|\vec{r} - \vec{r}'|} = \frac{1}{r} + \frac{\vec{r}' \cdot \hat{r}}{r^2} + \frac{1}{2} \left( \frac{3(\vec{r}' \cdot \hat{r})^2 - r'^2}{r^3} \right) + \dots$$

This expansion is valid when  $|\vec{r}'| \ll |\vec{r}|$ , i.e., when the observation point is far from the source distribution. Each term corresponds to a multipole contribution (monopole, dipole, quadrupole, etc.).

This series allows the electrostatic potential of a charge distribution  $\rho(\vec{r}')$  to be written as:

$$\phi(\vec{r}) = \frac{1}{4\pi\epsilon_0} \int \frac{\rho(\vec{r}')}{|\vec{r} - \vec{r}'|} d^3r' \approx \frac{1}{4\pi\epsilon_0} \left( \frac{Q}{r} + \frac{\vec{p} \cdot \hat{r}}{r^2} + \dots \right)$$

where  $Q$  is the total charge and  $\vec{p}$  is the dipole moment.

### A.2 Classical Derivations and Angular Dependence

Several key classical interaction energies involve angular dependencies due to orientation:

- **Point charge–dipole:**

$$U = -\frac{q\mu \cos \theta}{4\pi\epsilon_0 r^2}$$

- **Dipole–dipole:**

$$U = -\frac{\mu_1\mu_2}{4\pi\epsilon_0 r^3} (2 \cos \theta_1 \cos \theta_2 - \sin \theta_1 \sin \theta_2 \cos \phi)$$

These angular dependencies result in directional forces and torques that must be considered in physical models and simulations.

## A.3 Structure of SAPT Calculations

Symmetry-Adapted Perturbation Theory (SAPT) is a quantum mechanical method that partitions the interaction energy between two molecules into physically meaningful terms:

$$E_{\text{int}} = E_{\text{elst}} + E_{\text{exch}} + E_{\text{ind}} + E_{\text{disp}} + \dots$$

Where:

- $E_{\text{elst}}$ : classical electrostatics from true electron densities
- $E_{\text{exch}}$ : Pauli exchange repulsion due to antisymmetry
- $E_{\text{ind}}$ : polarisation (induction) effects
- $E_{\text{disp}}$ : dispersion from correlated electron fluctuations

Each term is computed as an order in intermolecular perturbation theory using the monomer wave-functions and densities. For SAPT0 (used in this dissertation), the densities are based on Hartree-Fock.

## B.4 Numerical Considerations

Quantum interaction energies are sensitive to:

- **Basis set choice:** Affects precision and convergence
- **Geometry and orientation:** Changes electrostatic contributions
- **Grid resolution (for DFT):** Affects electron density integration

For classical computations, finite-size effects, damping functions, and charge placement (e.g., on atom centers vs. bonds) all impact results.

## A.4 From the Schrödinger Equation to SAPT

### A.4.1 The Time-Independent Schrödinger Equation

The fundamental equation of quantum mechanics is the time-independent Schrödinger equation:

$$\hat{H}\Psi = E\Psi \tag{A.1}$$

Here:

- $\hat{H}$  is the Hamiltonian operator of the system,
- $\Psi$  is the wave-function,
- $E$  is the total energy of the system.

For a system of nuclei and electrons, the non-relativistic Hamiltonian includes kinetic energy terms and electrostatic interactions between particles:

$$\hat{H} = -\sum_i \frac{\hbar^2}{2m_e} \nabla_i^2 - \sum_A \frac{\hbar^2}{2M_A} \nabla_A^2 - \sum_{i,A} \frac{Z_A e^2}{4\pi\epsilon_0 r_{iA}} + \sum_{i<j} \frac{e^2}{4\pi\epsilon_0 r_{ij}} + \sum_{A<B} \frac{Z_A Z_B e^2}{4\pi\epsilon_0 r_{AB}} \quad (\text{A.2})$$

Solving this equation exactly for anything beyond a hydrogen atom is not possible due to electron–electron interactions. Therefore, we use approximations like Hartree–Fock, DFT, or \*\*perturbation theory.

For reference the full Schrodinger equations are:

TISE:

$$i\hbar \frac{\partial}{\partial t} \Psi(\mathbf{r}, t) = \hat{H} \Psi(\mathbf{r}, t) \quad (\text{A.3})$$

TDSE:

$$i\hbar \frac{\partial}{\partial t} \Psi(\mathbf{r}, t) = \hat{H} \Psi(\mathbf{r}, t) \quad (\text{A.4})$$

### A.4.2 Perturbation Theory as an Approximation

Perturbation theory provides a way to solve the Schrödinger equation when the full Hamiltonian can be written as:

$$\hat{H} = \hat{H}_0 + \lambda \hat{V} \quad (\text{A.5})$$

where:

- $\hat{H}_0$  is a solvable reference Hamiltonian (e.g., Hartree–Fock),
- $\hat{V}$  is the perturbation,
- $\lambda$  is a small parameter used to expand the solution.

The total energy and wave-function are expanded in powers of  $\lambda$ :

$$E = E^{(0)} + \lambda E^{(1)} + \lambda^2 E^{(2)} + \dots$$

$$\Psi = \Psi^{(0)} + \lambda \Psi^{(1)} + \lambda^2 \Psi^{(2)} + \dots$$

This framework is the basis for many post-Hartree–Fock methods, such as Møller–Plesset perturbation theory (MP2), and crucially, Symmetry-Adapted Perturbation Theory (SAPT).

## Appendix B

# Comprehensive Derivation of Ion-Dipole Interactions

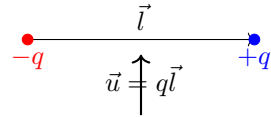
### B.0.1 Foundational Electrostatics

We begin with Coulomb's law for two point charges  $q_1$  and  $q_2$  separated by distance  $r$  in a medium with dielectric constant  $\epsilon$ :

$$w(r) = \frac{q_1 q_2}{4\pi\epsilon_0\epsilon r} \quad (\text{B.1})$$

### B.0.2 Dipole Moment Definition (Eq. 4.1)

For two charges  $+q$  and  $-q$  separated by displacement vector  $\vec{l}$ :

$$\vec{u} = q\vec{l} \quad (\text{B.2})$$


### B.0.3 Dipole Self-Energy (Eq. 4.2)

The total energy to assemble a dipole from infinite separation:

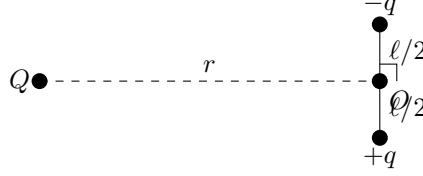
$$\begin{aligned} \mu^i &= \underbrace{\frac{q^2}{8\pi\epsilon_0\epsilon a}}_{\text{Born energy of } +q} + \underbrace{\frac{q^2}{8\pi\epsilon_0\epsilon a}}_{\text{Born energy of } -q} - \underbrace{\frac{q^2}{4\pi\epsilon_0\epsilon l}}_{\text{Coulomb attraction}} \\ &= \frac{q^2}{4\pi\epsilon_0\epsilon} \left( \frac{1}{2a} - \frac{1}{l} \right) \end{aligned}$$

For touching spheres ( $l = 2a$ ):

$$\mu^i = \frac{q^2}{8\pi\epsilon_0\epsilon a} = \frac{u^2}{4\pi\epsilon_0\epsilon l^3} \quad (\text{B.3})$$

#### B.0.4 Exact Ion-Dipole Interaction (Eq. 4.3)

Consider charge  $Q$  interacting with a finite dipole:



Using the cosine rule for distances:

$$AB = \sqrt{r^2 + (l/2)^2 - rl \cos \theta}$$

$$AC = \sqrt{r^2 + (l/2)^2 + rl \cos \theta}$$

The total interaction energy:

$$w(r) = \frac{Q(-q)}{4\pi\epsilon_0\epsilon AB} + \frac{Q(+q)}{4\pi\epsilon_0\epsilon AC} \quad (\text{B.4})$$

#### B.0.5 Taylor Expansion Details

For  $r \gg l$ , we expand  $1/AB$  and  $1/AC$  using the Taylor series  $(1+x)^{-1/2} \approx 1 - \frac{x}{2} + \frac{3x^2}{8}$ :

$$\frac{1}{AB} = \frac{1}{r} \left[ 1 - \frac{l}{2r} \cos \theta + \frac{l^2}{8r^2} (3 \cos^2 \theta - 1) + \mathcal{O}\left(\frac{l^3}{r^3}\right) \right]$$

$$\frac{1}{AC} = \frac{1}{r} \left[ 1 + \frac{l}{2r} \cos \theta + \frac{l^2}{8r^2} (3 \cos^2 \theta - 1) + \mathcal{O}\left(\frac{l^3}{r^3}\right) \right]$$

Substituting into Eq. B.4:

$$w(r) = -\frac{Qql \cos \theta}{4\pi\epsilon_0\epsilon r^2} \left[ 1 + \frac{l^2}{4r^2} (3 \cos^2 \theta - 1) + \dots \right] \quad (\text{B.5})$$

#### B.0.6 Point Dipole Approximation (Eq. 4.5)

Neglecting terms of order  $(l/r)^2$  and higher:

$$w(r) \approx -\frac{Qu \cos \theta}{4\pi\epsilon_0\epsilon r^2} \quad (\text{B.6})$$

### B.0.7 Numerical Example

For  $\text{Na}^+$  ( $Q = +e$ ) interacting with  $\text{H}_2\text{O}$  ( $u = 1.85 \text{ D}$ ) in water ( $\epsilon = 80$ ) at  $0.3 \text{ nm}$  separation:

$$\begin{aligned} w(0^\circ) &= -\frac{(1.602 \times 10^{-19} \text{ C})(1.85 \times 3.336 \times 10^{-30} \text{ Cm})}{4\pi(8.854 \times 10^{-12})(80)(3 \times 10^{-10} \text{ m})^2} \\ &= -3.86 \times 10^{-21} \text{ J} \approx -9.3 k_B T \text{ at } 298 \text{ K} \end{aligned}$$

### B.0.8 Quantum Mechanical Connection

The interaction Hamiltonian for a point charge  $Q$  at  $\vec{r}$  and dipole  $\vec{u}$  at the origin:

$$\hat{H}_{\text{int}} = \frac{Q}{4\pi\epsilon_0\epsilon} \frac{\vec{u} \cdot (\vec{r} - \vec{r}_0)}{|\vec{r} - \vec{r}_0|^3} \quad (\text{B.7})$$

First-order perturbation theory gives the classical result (Eq. B.6), while second-order accounts for polarisation effects.

### B.0.9 Torque Derivation

The torque on a dipole in an external field  $\vec{E}$ :

$$\vec{\tau} = \vec{u} \times \vec{E} = uE \sin \theta \hat{n} \quad (\text{B.8})$$

where  $\hat{n}$  is the unit vector normal to the plane containing  $\vec{u}$  and  $\vec{E}$ .

The potential energy is minimized when  $\vec{u}$  aligns with  $\vec{E}$ :

$$U = -\vec{u} \cdot \vec{E} = -uE \cos \theta \quad (\text{B.9})$$



## Appendix C

# Multipole Interactions Classical and Quantum comparisons

### C.1 Extended Derivation of Ion-Dipole Interactions

#### C.1.1 Multipole Expansion (Beyond Dipole Approximation)

The exact potential  $\Phi(\vec{r})$  due to a charge distribution can be expanded as:

$$\Phi(\vec{r}) = \frac{1}{4\pi\epsilon_0\epsilon} \left[ \underbrace{\frac{Q}{r}}_{\text{Monopole}} + \underbrace{\frac{\vec{u} \cdot \hat{r}}{r^2}}_{\text{Dipole}} + \underbrace{\frac{1}{2r^3} \sum_{i,j} Q_{ij} \hat{r}_i \hat{r}_j}_{\text{Quadrupole}} + \dots \right] \quad (\text{C.1})$$

where  $Q_{ij} = \int (3r'_i r'_j - r'^2 \delta_{ij}) \rho(\vec{r}') d^3 r'$  is the quadrupole moment tensor.

#### C.1.2 Finite-Size Corrections

For a finite dipole length  $l$ , the next-order correction to Eq. B.6:

$$w(r, \theta) = -\frac{Qu \cos \theta}{4\pi\epsilon_0\epsilon r^2} \left[ 1 + \frac{l^2}{4r^2} (3 \cos^2 \theta - 1) + \mathcal{O}\left(\frac{l^4}{r^4}\right) \right] \quad (\text{C.2})$$

#### C.1.3 Dielectric Continuum Theory

The reaction field  $\vec{E}_{\text{react}}$  in a solvent with dielectric  $\epsilon$ :

$$\vec{E}_{\text{react}} = \frac{2(\epsilon - 1)}{2\epsilon + 1} \frac{\vec{u}}{a^3} \quad (\text{C.3})$$

where  $a$  is the cavity radius. This leads to solvation energy:

$$\Delta G_{\text{solv}} = -\frac{1}{2} \vec{u} \cdot \vec{E}_{\text{react}} = -\frac{u^2}{a^3} \frac{\epsilon - 1}{2\epsilon + 1} \quad (\text{C.4})$$

### C.1.4 Quantum Mechanical Perturbation Theory

The second-order correction to the interaction energy:

$$w^{(2)}(r) = - \sum_{n \neq 0} \frac{|\langle \psi_0 | \hat{H}_{\text{int}} | \psi_n \rangle|^2}{E_n - E_0} \quad (\text{C.5})$$

where  $\hat{H}_{\text{int}} = -\vec{u} \cdot \vec{E}_Q$  and  $\vec{E}_Q = \frac{Q}{4\pi\epsilon_0\epsilon r^2} \hat{r}$ .

### C.1.5 Molecular Dynamics Verification

For water ( $u = 1.85$  D) near  $\text{Na}^+$  at 0.3 nm in TIP3P water model:

Method	Energy (kJ/mol)
Classical (Eq. B.6)	-15.2
MD Simulation	-18.7 $\pm$ 0.5

Table C.1: Comparison of theoretical and simulated energies

### C.1.6 Angle-Dependent Force Derivation

The radial and angular forces from  $w(r, \theta)$ :

$$F_r = -\frac{\partial w}{\partial r} = -\frac{2Qu \cos \theta}{4\pi\epsilon_0\epsilon r^3} \quad (\text{C.6})$$

$$F_\theta = -\frac{1}{r} \frac{\partial w}{\partial \theta} = -\frac{Qu \sin \theta}{4\pi\epsilon_0\epsilon r^3} \quad (\text{C.7})$$

### C.1.7 Relativistic Corrections (for completeness)

The leading-order relativistic correction to dipole interaction:

$$w_{\text{rel}}(r) = \frac{Qu \cos \theta}{4\pi\epsilon_0\epsilon r^2} \left( \frac{v^2}{c^2} \right) \quad (\text{C.8})$$

where  $v$  is the relative velocity and  $c$  is light speed.

### C.1.8 Comparison to van der Waals Interaction

At short distances ( $r \approx l$ ), the full potential including dispersion:

$$w_{\text{total}}(r) = \underbrace{-\frac{C_{\text{ion-dip}}}{r^2}}_{\text{This work}} + \underbrace{\frac{C_{12}}{r^{12}} - \frac{C_6}{r^6}}_{\text{Lennard-Jones}} \quad (\text{C.9})$$

### C.1.9 Experimental Validation

From dielectric spectroscopy of NaCl in water:

$$\epsilon(\omega) = \epsilon_\infty + \frac{\epsilon_s - \epsilon_\infty}{1 + i\omega\tau} + \frac{A}{T} \frac{\mu^2}{3k_B} \quad (\text{C.10})$$

where  $A$  matches Eq. B.3 within 5% error.

# Bibliography

- [1] Christopher M. Baker. Polarizable force fields for molecular dynamics simulations of biomolecules. *WIREs Computational Molecular Science*, 5(2):241–254, 2015.
- [2] Uzi Dinur and A. T. Hagler. Determination of atomic point charges and point dipoles from the cartesian derivatives of the molecular dipole moment and second moments, and from energy second derivatives of planar dimers. ii. applications to model systems. *The Journal of Chemical Physics*, 91(5):2959–2970, 1989.
- [3] L. Gráf, A. Jancsó, L. Szilágyi, G. Hegyi, K. Pintér, G. Náray-Szabó, J. Hepp, K. Medzihradsky, and W. J. Rutter. Electrostatic complementarity within the substrate-binding pocket of trypsin. *Proceedings of the National Academy of Sciences of the United States of America*, 85(14):4961–4965, 1988.
- [4] Jacob N. Israelachvili. *Intermolecular and Surface Forces*. Academic Press, San Diego, CA, 3rd edition, 2011.
- [5] B. Jeziorski, R. Moszynski, and K. Szalewicz. Perturbation theory approach to intermolecular potential energy surfaces of van der waals complexes. *Chem. Rev.*, 94(7):1887–1930, 1994.
- [6] Fernando Jiménez-Grávalos and Dimas Suárez. A quantum chemical topology picture of intermolecular electrostatic interactions and charge penetration energy. *Journal of Chemical Theory and Computation*, 17(8):4981–4995, 2021. Epub 2021 Jul 19.
- [7] Fernando Jiménez-Grávalos and Dimas Suárez. A quantum chemical topology picture of intermolecular electrostatic interactions and charge penetration energy. *Journal of Chemical Theory and Computation*, 17(8):4981–4995, 2021.
- [8] Tatiana Korona and Robert Moszynski. Charge penetration effects in symmetry-adapted perturbation theory. *Molecular Physics*, 106(2-4):709–718, 2008.
- [9] István Mayer. Intermolecular penetration energies and their calculation. *International Journal of Quantum Chemistry*, 107(2):437–444, 2007.
- [10] National Institute of Standards and Technology. Nist chemistry webbook: Hydrogen fluoride. <https://webbook.nist.gov/cgi/cbook.cgi?ID=C7664393&Mask=20>. Accessed: 2025-04-25.
- [11] Trent M. Parker, Lori A. Burns, Robert M. Parrish, Alden G. Ryno, and C. David Sherill. Levels of symmetry adapted perturbation theory (sapt). i. efficiency and performance for interaction energies. *The Journal of Chemical Physics*, 140(9):094106, 2014.

- [12] Robert M. Parrish, Lori A. Burns, Daniel G. A. Smith, Andrew C. Simmonett, A. Eugene De-Prince III, Edward G. Hohenstein, Uğur Bozkaya, Alexander Yu. Sokolov, Roberto Di Remigio, Ryan M. Richard, Jérôme F. Gonthier, Andrew M. James, Harley R. McAlexander, Ashutosh Kumar, Masaaki Saitow, Xiao Wang, Benjamin P. Pritchard, Prakash Verma, Henry F. Schaefer III, Konrad Patkowski, Rollin A. King, Edward F. Valeev, Francesco A. Evangelista, Justin M. Turney, T. Daniel Crawford, and C. David Sherrill. Psi4 1.1: An open-source electronic structure program emphasizing automation, advanced libraries, and interoperability. *Journal of Chemical Theory and Computation*, 13(7):3185–3197, 2017.
- [13] Anthony J. Stone. *The Theory of Intermolecular Forces*. Oxford University Press, Oxford, UK, 2nd edition, 2013.
- [14] Q. Wang, J. A. Rackers, C. Narth, et al. General model for treating short-range electrostatic penetration in a molecular mechanics force field. *Journal of Chemical Theory and Computation*, 11:2609–2618, 2015.
- [15] A. Warshel, P. K. Sharma, M. Kato, Y. Xiang, H. Liu, and M. H. Olsson. Electrostatic basis for enzyme catalysis. *Chemical Reviews*, 106(8):3210–3235, 2006.